FLUID DYNAMICS OF NON-NEWTONIAN THIN FILMS: SQUEEZING FLOW, FILM RUPTURE AND CONTACT LINE INSTABILITY

BY

Md. Rajib Anwar

Submitted to the graduate degree program in Bioengineering and the Graduate Faculty of the University of Kansas in partial fulfillment of the requirements for the degree of Doctor of Philosophy

---
Chairperson Dr. Sarah Kieweg

Co-chairperson Dr. Kyle Camarda

Dr. Sara Wilson

Dr. P. Scott Hefty

Dr. Xuemin Tu

Date Defended: June 7th, 2016

The dissertation committee for Md. Rajib Anwar

certifies that this is the approved version of the following dissertation:

FLUID DYNAMICS OF NON-NEWTONIAN THIN FILMS: SQUEEZING FLOW, FILM RUPTURE AND CONTACT LINE INSTABILITY

Chairperson Dr. Sarah Kieweg

Co-chairperson Dr. Kyle Camarda

Date Approved: June 13th, 2016

ABSTRACT

HIV is a global pandemic that affects millions of lives every year. Vaginal gel formulation has been touted as an effective strategy to fight sexually transmitted diseases (STD) by acting as a physical barrier, and also by delivering active pharmaceutical agents at the intended location. Microbicidal gels can act as a low cost, self-administered method to prevent HIV and other STD's. The overall long term goal of our research group is to rationally design these delivery vehicles by optimizing their rheological properties for their specific applications. In that regard, there has been an ongoing effort in our group to mathematically model the flow of thin films in order to understand the dynamics and stability of these films, so that we can understand/predict the behavior of the gel during their applications. In my dissertation, I have used thin film lubrication theory to develop mathematical models of (a) boundary elasticity-driven squeezing flow of yield stress fluids, (b) rupture/dewetting of Ellis-type shear-thinning liquid films, and (c) contact line instability of Ellis-type shear-thinning liquid films. Our investigations showed that yield stress can improve the control over the spreading characteristics of liquids, and also possibly aid in the retention of liquid in place. We have demonstrated an optimization framework that can be used to estimate the rheological properties of microbicidal gels for different combinations of tissue elasticity, initial bolus volume, and deployment time. Numerical models of the rupture and dewetting of Ellis-type thin films showed that the shear-thinning rheology could accelerate the rupture process which could create dry spots earlier than Newtonian fluids. Dry spots are usually unwanted for both functional and aesthetic purposes. Numerical models of contact line instability have shown that the shear-thinning rheology increases the finger growth rate for vertical inclines but shows a more complex behavior for flatter inclines. For flatter inclines, the most unstable mode shifts to larger wavelength but the finger growth rate is dependent on the degree of shear-thinning. Fluids with low degree of shear-thinning suppress the fingering but fluids with the highest degree of shear-

thinning show an increased growth rate despite the shift in the most unstable mode to larger wavelength. This behavior possibly occurs due to the decrease of apparent viscosity far beyond contact line, especially for fluids with a narrow range for the Newtonian plateau. Lubrication theory can be applied in the modeling of numerous biological and industrial applications. The models developed here are not limited to any specific application, and can easily be modified to study other applications that involves non-Newtonian fluids.

ACKNOWLEDGEMENTS

I am extremely grateful to Dr. Sarah Kieweg, and Dr. Kyle Camarda for their support and guidance which has made this work possible. I am indebted to them for successfully completing this research work. I would like to express my deepest thankfulness to my supervisor, Dr. Kieweg for helping me to overcome the difficulties associated with my research and for her valuable advice all along my PhD. I express my deepest gratitude to Dr. Sara Wilson, Dr. P. Scott Hefty and Dr. Xuemin Tu for being in my committee.

I am also thankful to my colleagues and friends, Bin Hu, Brock Roughton, Thora Whitmore, Zouhair Talbi, and Kyle Boone for their support. I am grateful to Bin Hu for helping me with my research and providing valuable suggestions about this work. I would like to thank my parents and my wife, Farhana Abedin for supporting me all along my PhD and giving me the inspiration to successfully complete the steps of my PhD degree.

I would also like to thank Dr. Kam Ng, Dr. Dennis Perchak and Dr. Bradley Coltrain for their mentoring and guidance during my internship at Eastman Kodak. I have learned a lot about interfacial fluid dynamics at Kodak, and applied some of the numerical techniques learned there in my dissertation research.

I would also like to acknowledge my gratefulness to Denise Bridwell for helping me with various administrative processes while I was a PhD student at the University of Kansas. This work was supported by the research grant from National Institutes of health (NIH), Grant # R21/R33 AI082697 (from the National Institute of Allergy and Infectious Diseases)

CONTENTS

LIST OF FIGURES

LIST OF TABLES

Chapter 1

INTRODUCTION

1.1 Overview and Objective

Study of the dynamics of “thin film flow” is critical for designing effective anti-HIV microbicides that are intended to be used in a complex biophysical environment. Thin film flows or coating flows have been studied for various biological, geological and industrial applications such as microbicidal drug delivery [1-6], lung surfactants [7], synovial fluids [8], tear films [9, 10], mud flow [11], lava flow [12], industrial paint/coating flows [13-15], etc. The study of thin Newtonian liquid films (e.g. spreading, rupture, contact line instability) has been the subject of extensive investigation for many years [16-18]. However, non-Newtonian rheology (shear-thinning, yield stress) plays an important role in the overall flow dynamics and instability of non-Newtonian fluids. There is a definite gap in knowledge in terms of understanding the behavior of non-Newtonian thin film dynamics and instability. These gaps hinder the design of effective delivery vehicles for microbicide deployment.

Our long term goal is to use the knowledge of fluid mechanics and polymer rheology to simulate the physical behavior of drug delivery systems in complex environments, and to apply this knowledge in designing delivery vehicles containing STI preventive and/or therapeutic agents. The objective of this dissertation is to investigate the effect of non-Newtonian rheology on three

different scenarios involving thin films: squeezed film flow, film rupture/dewetting, and contact line instability. The overall hypothesis of this project is that non-Newtonian rheology of thin films can be used as important design variables for the development of microbicide gels, and mathematical modeling of non-Newtonian thin film dynamics can help in understanding the behavior of the delivery vehicles *in-vivo*. The rationale for the proposed research is that, once the dynamics of non-Newtonian thin films are clearly understood, we can make informed decisions about designing the delivery vehicles.

We accomplished our objectives through studies performed under 3 specific aims:

1. **Mathematical modeling of tissue elasticity and gravity-driven squeezing flow of microbicidal gels and optimization of rheological properties.**

   The approach involved developing a partial differential equation describing the tissue elasticity and gravity-driven flow of non-Newtonian microbicidal gels and optimizing the spreading and retention of a gel on epithelial surfaces. The hypothesis was that rheological properties of gels can be numerically optimized to achieve optimal coverage and retention behavior. This is important because it indicates that yield stress of gels can improve the retention of the gel on the vaginal epithelial surface.

2. **Mathematical modeling of rupture and dewetting of Ellis-type liquid thin films.**

   The approach involved developing a mathematical model of thin film rupture/dewetting of shear-thinning fluids and numerically solving the problem to get the rupture time, and investigating the effect of shear-thinning rheology on the preferred mode of instability. The hypothesis was that shear-thinning of a liquid will cause a different rupture time than Newtonian thin films and hence affect the function of the film as a physical barrier.

3. **Mathematical modeling of contact line instability of gravity-driven flow of shear-thinning Ellis liquid films.**

The approach involved developing a mathematical model for contact line instability of shear-thinning fluid films and exploring the effect of shear-thinning (via Ellis rheological model) on contact line instability through linear stability analysis (LSA) and nonlinear simulation. The hypothesis was that the shear-thinning behavior of a fluid will likely affect the contact line instability due to the change in capillary ridge height and/or apparent viscosity change.

1.2 Significance of Proposed Research in Microbicide Development

The impact of the expanding HIV/AIDS pandemic is devastating. There were approximately 34 million people living with HIV in 2012 – including 2.5 million new infections in 2011 alone [19]. Studies designed to determine the effect of treating sexually transmitted infections (STIs) from pathogens such as *C. trachomatis* and *N. gonorrheae*, on HIV transmission rates support that STI prevention and management is an effective strategy [20, 21]. Clinical trials of a vaginal gel formulation of anti-retroviral drug Tenofovir exhibited the potential of topically applied gel for the prevention of HIV transmission in women [22]. Microbicidal gels could be a self-administered and inexpensive method to prevent transmission of HIV and other STIs in women. In addition to acting as delivery vehicles for anti-HIV and other anti-STD agents, the microbicidal gels could also act as physical barriers between pathogens and biological tissues. Factors such as extent of coating and its retention on the epithelial surface of the lower female reproductive tract (LFRT) play a vital role in the effectiveness of the gel against transmission of HIV and STD [23]. The microbicide development strategy (MDS) has identified gaps in knowledge for microbicide development which includes a lack of knowledge in the vehicle design [24]. Vehicle design is a problem with multiple facades including gel rheology optimization, biocompatibility, user acceptability and anti-STI activity. This project focuses on studying the dynamics of fluid that may be encountered in a microbicidal gel deployment situation using the principles of interfacial and thin film flow. Previous research has shown that typical polymeric gel formulations exhibit

shear-thinning behavior and may also have a yield-stress [25-27]. Despite the advances in the area of mathematical modeling of thin film flow, there is still lack of knowledge in the field of non-Newtonian liquid film flow.

Our contribution here is to investigate the effect of non-Newtonian rheology on the dynamics and stability of thin films. The contribution is significant because it is expected to provide us with strong mathematical tools to predict the dynamics of non-Newtonian liquid films. This knowledge can be applied to the design of effective delivery vehicles. Due to the numerous applications of thin films in biological and industrial applications, these computational models will also inform researchers involved in other fields (especially in micro-printing and coating applications) about the important consequences of non-Newtonian rheology on thin film dynamics. These models will also serve as platforms for building more complicated models by including detailed contact line physics, evaporation, complex rheology, surface patterning/flexibility etc.

1.3 Review of Relevant Literature

Thin film flows can be mathematically described by using the thin film lubrication approximation which enables us to neglect the inertial effects [28]. There has been a progressive development in the study of thin films for various problems involving thermocapillary flow, coating flow, phase change at interface, film drainage etc. The majority of the studies involving thin film flow have been conducted on Newtonian fluids. The Carreau, power-law, and Ellis models are some popular constitutive equations that can be used to describe the shear-thinning behavior of non-Newtonian fluids. Bingham (Newtonian with yield strength) and Herschel-Bulkley (shear-thinning with yield strength) constitutive equations are commonly used to represent fluids having yield strength.

Thin film spreading and retention depends on the rheological properties of the fluid. Thin film theory has been applied in the study of vaginal drug delivery systems by several researchers in the recent past. Kieweg and Katz *et al.* performed experimental and numerical studies on microbicidal gel deployment under constant squeezing force and concluded that squeezing force, gel consistency, shear-thinning behavior and yield stress are strong determinants of the coating performance of gels [23, 25, 26]. Szeri *et al.* developed a mathematical model involving wall elasticity to demonstrate the effect of the compliant vaginal wall on the deployment dynamics of microbicidal gels and indicated the important role that vaginal biomechanics played in gel deployment [4]. Tasoglu *et al.* showed that yield stress could improve the long time retention performance of a Carreau-like fluid [6]. These studies were clear indicators that fluid spreading and retention could be rationally controlled by optimizing the rheological properties of the fluid. However, there is a definite lack of any squeezing flow model of yield-stress fluid that describes the short term deployment dynamics of microbicide gels. To close this gap, we have (a) developed a mathematical model for understanding the effect of elasticity of the tissue and yield-stress rheology of the fluid on the spreading of microbicidal gels, and (b) demonstrated an optimization framework to estimate gel rheological properties for a given tissue elasticity in order to achieve both optimal tissue coverage and maximum retention.

Research on the spontaneous rupture and dewetting of thin films has been motivated by various biological and industrial needs [29-33]. In thin films where surface tension plays an important role, a small perturbation of the interface shape can grow and eventually result in the rupture of the film. Rupture is the process where the film thickness approaches zero at a finite time point. The subsequent spatial growth of the minimum height, which forms dry spots in the liquid film is known as dewetting. Early theoretical works have predicted the rupture time and length-scale of preferred mode of instability of thin films of Newtonian fluids [17, 34]. The most unstable mode is defined as the wavelength at which the initial disturbance grows most rapidly,

and is the most likely initial spacing between mounds or ridges for a randomly imposed perturbation. However, a number of these studies used a simplified model of disjoining pressure (the dynamic pressure arising from solid/fluid interaction at molecular level) that allowed the model to represent the film evolution only up to the point of film rupture. Later works have used a more complex model of disjoining pressure that allowed the modeling of the dewetting process followed by rupture [35]. The growth rate of initial disturbance has been shown to be proportional to surface tension and the contact angle, and inversely proportional to the film thickness and viscosity in Newtonian fluids [35]. The wavelength of the most unstable mode (preferred mode) of instability has been shown to be proportional to the film thickness and inversely proportional to the contact angle [35]. Researchers have investigated the rupture/dewetting behaviors of evaporating films [17, 36], films with trapped nano-bubbles [37], and colloidal suspension [38]. Evaporation (condensation) leads to faster (slower) growth of initial disturbance [17]. Presence of nano-scale bubbles has also been shown to accelerate the rupture process [37]. Dewetting models of evaporating colloidal suspension has been developed to explain the self-pinning of receding contact line which is related to the formation of rings of dried particles, also known as the “coffee ring” effect [38]. Most of the above studies have considered a Newtonian fluid behavior. However, the rheological behavior of many industrial and biological fluid exhibit shear-thinning behavior. To address this gap in knowledge, we have addressed the rupture and dewetting behavior of Ellis-type fluids that exhibits a low shear rate Newtonian plateau along with shear-thinning behavior at high shear [39].

Effects of shear-thinning on contact line instability of thin liquid films have not been fully characterized yet. Contact line instability which causes the formation of fingers downstream has been widely studied for Newtonian fluids by various researchers [16, 40-42]. Random perturbation at the contact line can cause the moving front to corrugate, and this behavior is a function of both surface tension and inclination angle [43]. Formation of fingers at the moving front is undesirable

since it may lower the quality of coating or negatively affect the barrier properties by leaving dry spots. Therefore, contact line instability is very important in any coating application. Yield-stress has been shown to suppress contact line instability [44]. Our group has already performed numerical investigation on the effect of power-law rheology on contact line instability and the results showed that shear-thinning suppresses fingering instability [45]. However, the power-law model predicts an unrealistic infinite viscosity at low shear rates and this behavior may have an impact on the contact line instability. Therefore, we have chosen to subsequently study the contact line instability phenomena using the Ellis fluid model which has a more robust representation of shear-thinning fluids through the inclusion of a low shear rate Newtonian plateau. To strengthen our current knowledge on the effects of non-Newtonian rheology on contact line instability, we have developed mathematical models of the spreading of Ellis fluids, and investigated the effect of shear-thinning on contact line instability by performing linear stability analysis and non-linear simulation.

Collective evidence reviewed in this section strongly supports the conclusion that there is a definite lack of knowledge in terms of mathematically explaining the behavior of non-Newtonian thin film flows. This knowledge is important as it will help in the development and optimization of various industrial processes, the understanding of biological phenomena and in our effort to develop microbicidal delivery vehicles of non-Newtonian fluids.

1.4 Thin Film (Lubrication) Approximation

Lubrication flow is a common phenomenon observed in our day to day life such as application of eye drops or microelectronic printing. Here, the basis of thin film flow is discussed. Please see reference [28] for further details. A viscous fluid between two rigid boundaries ($z = 0$ and $z = h(x, y)$) with a steady flow is considered here. Let U be the horizontal flow speed and L

be the horizontal length scale for the flow. We start with the incompressible Navier-Stokes equation, and the continuity equation:

$$\rho\left(\vec{u}_t + \vec{u} \bullet \nabla\vec{u}\right) = -\nabla p + \rho g + \eta\nabla^2\vec{u} \tag{1.1}$$

$$\nabla \bullet \vec{u} = 0$$

Here, ρ is density, g is gravitational acceleration, η is dynamic viscosity, $\vec{u}$ is the velocity vector, and p is pressure. In this discussion, a two dimensional flow is considered to be one dimensional when the longitudinal dimension is significantly longer than the transverse dimension as given below.

$$h << L \tag{1.2}$$

Since there will be no slip condition at the boundaries (*z = 0* and *z = h*), then *u* will vary by an order of *U* over a distance of order *h* in the *z*-direction. Therefore, the longitudinal gradients of *u*, $\partial u/\partial z$ and $\partial^2 u/\partial z^2$ will be of the order U/h and U/h^2 respectively. Similarly, the horizontal gradients of *u*, $\partial u/\partial x$ and $\partial^2 u/\partial x^2$ will be of the order U/L and U/L^2 respectively and they are weaker compared to that in the longitudinal direction. Considering the above equation, the viscous term can be approximated as shown below:

$$\nu\nabla^2 u \approx \nu\frac{\partial^2 u}{\partial z^2} \tag{1.3}$$

Here, $\nu = \eta/\rho$ is the kinematic viscosity. The order of magnitude of the two components of the two terms in the equation of motion can be estimated as given below:

$$(u \bullet \nabla)u \approx \frac{U^2}{L}(1,1,\frac{h}{L}) \tag{1.4}$$

$$\nu \frac{\partial^2 u}{\partial z^2} \approx \frac{\nu U}{h^2}(1,1,\frac{h}{L}) \tag{1.5}$$

Due to the incompressibility of the fluid, the continuity equation is $\nabla \bullet \vec{u} = 0$. Since, $\partial w/\partial z$ is of the order U/L, w is of the order Uh/L. Taking into account these estimates, $(u.\nabla)u$ can be neglected if the following equation is satisfied.

$$\frac{UL}{\nu}(\frac{h}{L})^2 << 1 \tag{1.6}$$

From the above equation, it can be seen that the conventional Reynolds number $\mathrm{Re} = UL/\nu$ does not need to be low. The thin film theory is based on that the inertial force is either comparable or lower than the viscous force. Even when the Reynolds number is large, the condition in the above equation can be satisfied, allowing the viscous force to dominate if only h/L is low enough.

1.5 Innovation

This work is innovative and original because (a) it models the squeezing flow dynamics of yield-stress fluid, (b) it investigates the rupture instability of Ellis-type thin films for the first time, and (c) it investigates the contact line instability of Ellis-type shear-thinning fluid films for the first time. Overall, this knowledge will help us to achieve predictable coating behavior in important biological and industrial applications. The research outcomes are significant to microbicide development as well because they will aid in the design of effective delivery vehicles.

Chapter 2

MATHEMATICAL MODELING OF TISSUE ELASTICITY AND GRAVITY-DRIVEN SQUEEZING FLOW OF MICROBICIDAL GELS AND OPTIMIZATION OF RHEOLOGICAL PROPERTIES

The contents of this chapter was published in Md Rajib Anwar, Kyle V. Camarda, and Sarah Kieweg (2015). "Mathematical model of microbicidal flow dynamics and optimization of rheological properties for intra-vaginal drug delivery: role of tissue mechanics and fluid rheology". Journal of Biomechanics, 48(9), 1625-1630.

2.1 Introduction

Recent clinical trials of the vaginal gel formulation of the anti-retroviral drug Tenofovir have shown the efficacy of topically applied microbicidal gels against HIV transmission to women [22] Microbicidal gels could provide us with a self-administered and low cost strategy to fight HIV and other sexually transmitted infections (STIs). A microbicidal gel is deployed as a delivery vehicle of anti-HIV and other anti-STI agents, and it is also used to act as a physical barrier between the pathogens and the biological tissue. The efficacy of a microbicidal gel depends on the extent of coating and retention on the epithelial surface of the lower female reproductive tract (LFRT) [23]

The coating mechanism of a microbicidal gel is complex in nature and driven by the combined effect of physical mechanisms in the LFRT and the rheological properties of the gel. Gravity and the squeezing force arising from the elasticity of vaginal tissue are physical mechanisms that play important roles in the coating mechanism. Variation of the elasticity of vaginal tissue can change the extent of coating of these gels due to different magnitudes of the resulting squeezing force. These polymer gels usually exhibit shear-thinning behavior and may also have a yield stress [25-27]. Certain important anatomical and physiological features of the vaginal environment, such as pH, volume and composition of vaginal fluid, should be kept in mind while designing an effective microbicidal gel. The long term goal of our research is to develop a framework for rational design of microbicide gels with active ingredients. As a step towards achieving that goal, we have used squeezing flow mechanics and polymer rheology to develop a framework for optimizing the gel rheological properties to achieve optimal spreading and retention which may be further extended later by incorporating target properties such as biocompatibility and activity against STIs.

Studies on thin film flows for biological applications are growing in number [8]. Most common biological applications include lining of pleural surfaces of the lung [7], flow of synovial fluid between joints [8], and tear film between the eye and eyelid [9, 10]. Thin film theory has been applied in the study of vaginal drug delivery systems by several researchers in recent past. Kieweg and Katz *et al.* performed experimental and numerical studies on microbicidal gel deployment under constant squeezing force and concluded that squeezing force, gel consistency, shear-thinning behavior and yield stress were strong determinants of the coating performance of gels [23, 25, 26]. Szeri *et al.* developed a mathematical model involving wall elasticity to demonstrate the effect of compliant vaginal wall on the deployment dynamics of microbicidal gels and indicated the important role that vaginal biomechanics played in gel deployment [4]. Tasoglu *et al.* showed that yield stress could improve the long time retention performance of a Carreau-

like fluid [6]. The goal of this study is (a) to develop a mathematical model for understanding the effect of elasticity of the tissue and yield-stress rheology of the fluid on the spreading of microbicidal gels, and (b) to demonstrate an optimization framework to estimate gel rheological properties for a given tissue elasticity in order to achieve both optimal tissue coverage and maximum retention.

2.2 Problem Formulation

In this section, we develop the nonlinear partial differential equation that describes the evolution of the fluid/solid interface as a function of time and space, $h(x,t)$. Figure 2.1 shows the schematic of the flow conditions of the two dimensional (2-D) model i.e. one dimensional (1-D) spreading, where the fluid is spreading due to the gravity and an elastic response from the vaginal tissue. This model considers a homogenous tissue compartment which represents the entire vaginal tissue (including epithelium, smooth muscular layers, and the underlying lamina propria), as well as further surrounding/underlying structures which may contribute to the closing pressures exerted on the gel in the vagina (e.g. nearby bladder wall). The flow domain is symmetric about the center axis since we are considering only vertical flow (along x-direction) in this study. In this approximation, the portion of the vaginal axis shown in Figure 2.1 is aligned with the x-axis, and gravity is downhill along the x-axis. In a human, the orientation of the vaginal axis with respect to the gravity depends on both the location along the s-shaped vaginal axis and the orientation of the woman. The axis orientation in this model allows consideration of the full range of the impact of gravity on a gel.

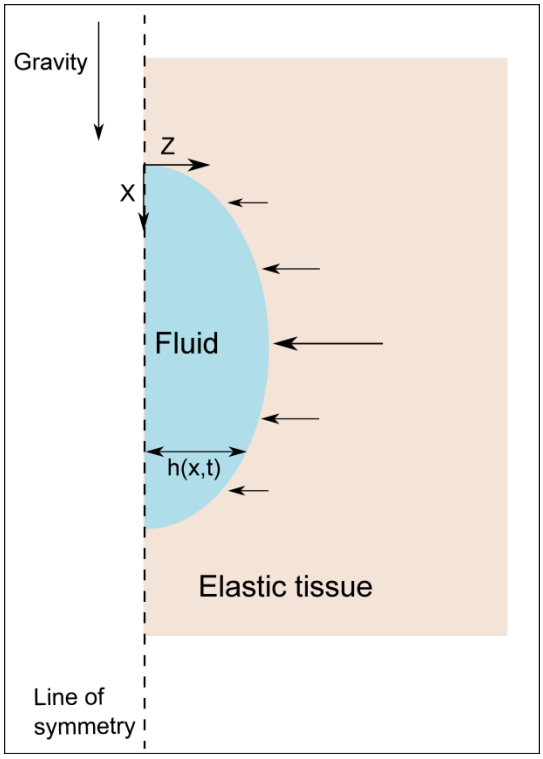

Figure 2.1. A schematic representation of the fluid bolus in vaginal canal (drawing is not to scale). Only half plane is shown due to symmetry. The vaginal introitus at the canal opening is towards the bottom. This simplified two dimensional model assumes that the vaginal canal is perfectly aligned with the x-axis. Placing a constant volume bolus distends the tissue surfaces. This serves as the initial state of our model. Flow starts immediately due to the combined effect of gravity and boundary squeezing pressure from the elastic tissue.

Since the thickness of the gel bolus is much smaller than the extent of the spreading, the thin film lubrication approximation [28] allows us to neglect the convective terms in the equations of conservation of linear momentum. The Herschel-Bulkley constitutive law which is used to represent the rheology of a yield stress fluid is as follows:

$$\tau_{zx} = \tau_0 + m\left|\frac{\partial u}{\partial z}\right|^{n-1}\frac{\partial u}{\partial z} \tag{2.1}$$

Here τ_{zx} is the shear stress, τ_0 is the yield stress, u is the velocity in the x-direction, m is the consistency and n is the power-law index. The elasticity of the vaginal wall is incorporated in the pressure term of the model. A linear elastic tissue behavior is considered which assumes that the vaginal wall is homogeneous and isotropic, and the pressure p acting on the fluid boundary due to the tissue elasticity is directly proportional to strain in the distensible tissue. The pressure for a deformation $h(x,t)$ is given by $p = E \cdot \in = E \cdot h(x,t)/T$ [4]. Here, E is the elastic modulus of the tissue, T is the thickness of the tissue layer and $\in = h(x,t)/T$ is the strain in the tissue. We apply a no-slip condition at the fluid-solid interface and zero shear stress at the symmetry line.

By using the above pressure formulation, thin film approximation, and Herschel-Bulkley constitutive relation, we arrive at the following nonlinear partial differential equation describing the evolution of the fluid-solid interface.

$$\frac{\partial h}{\partial t} + \frac{\partial}{\partial x}\left[\left(\frac{1}{m}\right)^n\left(\frac{n}{1+n}\right)\left(\frac{n}{1+2n}\right)\left(\frac{E}{T}\frac{\partial h}{\partial x} - \rho g\right)\left|\frac{E}{T}\frac{\partial h}{\partial x} - \rho g\right|^{\frac{1}{n}-1} Y^{\frac{1+n}{n}}\left(Y - \left(\frac{1+2n}{n}\right)h\right)\right] = 0 \tag{2.2}$$

$$Y = \max\left(h - \frac{\tau_0}{\left|\frac{E}{T}\frac{\partial h}{\partial x} - \rho g\right|}, 0\right)$$

Here, Y defines the yield surface. See Appendix A2 for details of the derivation. The surface, $z = Y(x,t)$ separates a shearing flow region (between the yield surface and the vaginal wall) and the adjacent plug region. This central plug region is not a true plug, but rather a weakly yielding zone

[46]. For a constant volume spreading such as in our case, a no-flux boundary condition ($\partial h/\partial x = 0$) was applied at the two ends of the spatial domain which was taken large enough to ensure that the fluid would not reach the ends.

Previous literature reported that the extent of gel coating increases with the increase of $E\ and\ n$, and decreases with the increase of $m\ and\ \tau_0$ [4, 26]. In order to understand the interplay between the tissue's elastic properties and the fluid's yield stress on the deployment dynamics, we use appropriate scaling to create a non-dimensional evolution equation for the fluid/solid interface ($\bar{x} = x/L$, $\bar{h} = h/H$, $\bar{t} = tU/L$, $\bar{P} = P/\rho gT$ and $\bar{\tau}_{xz} = \tau_{xz}/\rho gH$, where $U = H^{\frac{1}{n}+1}(\rho g/m)^{\frac{1}{n}}$ is the characteristic flow velocity).

$$\frac{\partial \bar{h}}{\partial \bar{t}} + \frac{\partial}{\partial \bar{x}}\left[\left(\frac{n}{1+n}\right)\left(\frac{n}{1+2n}\right)\left(EG\frac{\partial \bar{h}}{\partial \bar{x}} - 1\right)\left|EG\frac{\partial \bar{h}}{\partial \bar{x}} - 1\right|^{\frac{1}{n}-1}\bar{Y}^{\frac{1+n}{n}}\left(\bar{Y} - \left(\frac{1+2n}{n}\right)\bar{h}\right)\right] = 0 \tag{2.3}$$

$$\bar{Y} = \max\left(\bar{h} - \frac{Bi}{\left|EG\frac{\partial \bar{h}}{\partial \bar{x}} - 1\right|}, 0\right)$$

This non-dimensional form provides us with two important dimensionless variables: the yield stress to gravity ratio $Bi = \tau_0/\rho gH$, and the tissue elasticity to gravity ratio $EG = E \in/\rho gL$. Here, H and L are the characteristic lengths along the height and flow direction. A dimensional interpretation, along with approximate dimensional values for tissue elasticity and gel properties, will be discussed in the Results and Discussion section.

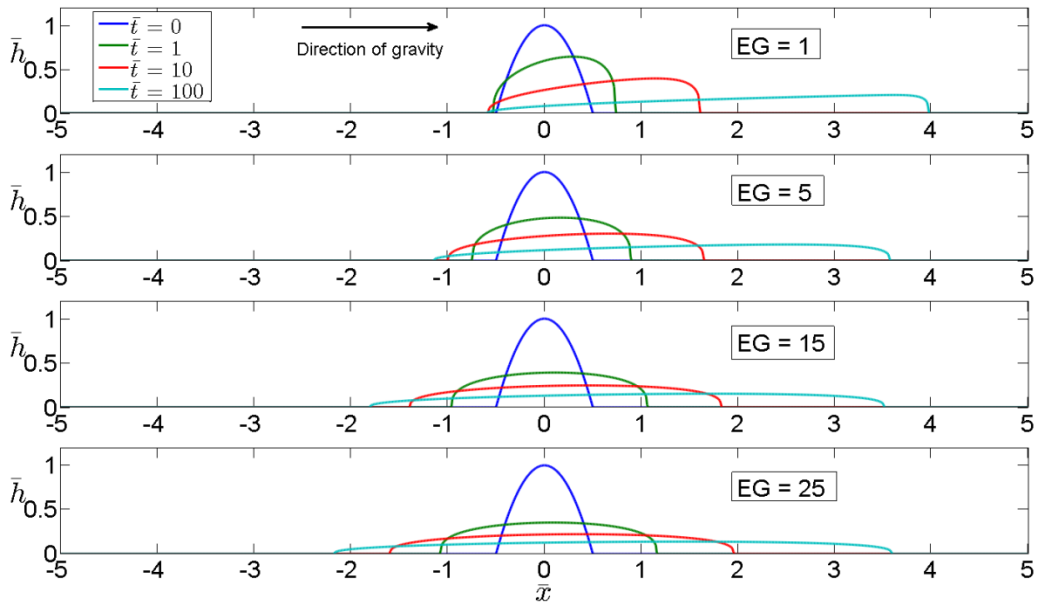

Figure 2.2. Effect of wall elasticity on the spreading of bolus. *EG* ratios used for simulation are 1, 5, 15 and 25. Plots are shown at $\bar{t}$ = 0, 1, 10 and 100. The value of *Bi* = 0 and *n* =1 used for all simulations. At low *EG*, the flow is mostly downward due to the dominance of gravity. Higher *EG* increases the coating length and also causes noticeable upward flow.

In the rest of the chapter, we first explore the effects of varying tissue elasticity and yield stress by solving the non-dimensional form of the evolution equation for different ranges of these parameters. The nonlinear evolution equation was solved by an implicit finite difference scheme which is similar to the technique used in our previously published research [1-3]. We used first order backward difference in time and second order central difference in spatial derivatives. Newton's method was used to solve the system of algebraic equations resulting from the discretization. A spatial mesh interval dx = 0.01 and an adaptive time-stepping scheme was used to match our tolerance requirement of 1e-6 (default time-step size was set to dt = 0.001). We also monitored the volume of fluid since insufficient spatial or temporal resolution resulted in a violation

of mass conservation. Next, we demonstrated a framework for optimizing the gel rheological properties by leveraging the yield stress of the gel for a given tissue elasticity. Optimization methods are described below in the analysis contained in the Results and Discussion section.

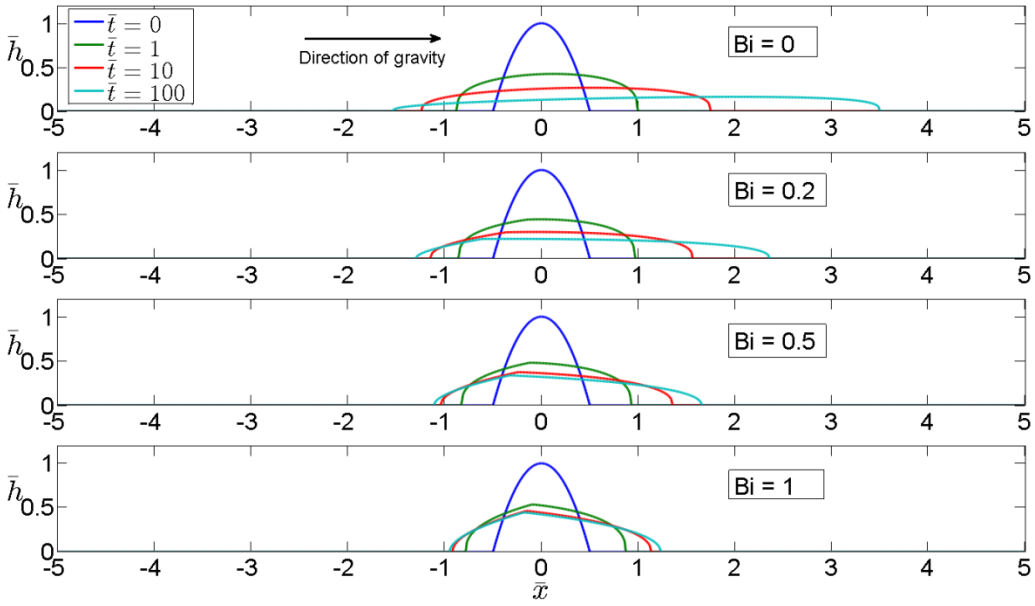

Figure 2.3. Effect of yield stress on the spreading of bolus. *Bi* ratios used for simulation are 0, 0.2, 0.5 and 1. Plots are shown at $\bar{t}$ = 0, 1, 10 and 100. The value of *EG* = 10 and *n* =1 used for all simulations. Increase in the yield stress (increase in *Bi*) reduces the coating length.

2.3 Results and Discussion

Rheological properties of gels and elasticity of tissue are required as input parameters of the mathematical model. Based on measured properties of some commercial gels, a reasonable range of rheological properties could be considered as following: m = 10-80 Pa-s^n, n = 0.25-1.0 and τ_0 = 0-100 Pa [23, 25]. Exact elasticity of vaginal tissue is still unknown and wide ranges of

elasticity such as 3-10 kPa [47], and 12-36 kPa [48] are reported. The length of the vaginal canal can range from 7-10 cm, with a wall thickness between 0.5-2.0 cm [4, 49]. For our numerical simulation, a constant tissue thickness of T = 1.5 cm was considered and represented the entire vaginal wall and the effect of surrounding tissues. The initial bolus shape was parabolic (see Fig. 2.1) with a length L = 4 cm and maximum height H = 0.3 cm. This configuration yields a bolus volume of 1.6 ml/width dimension of the vagina.

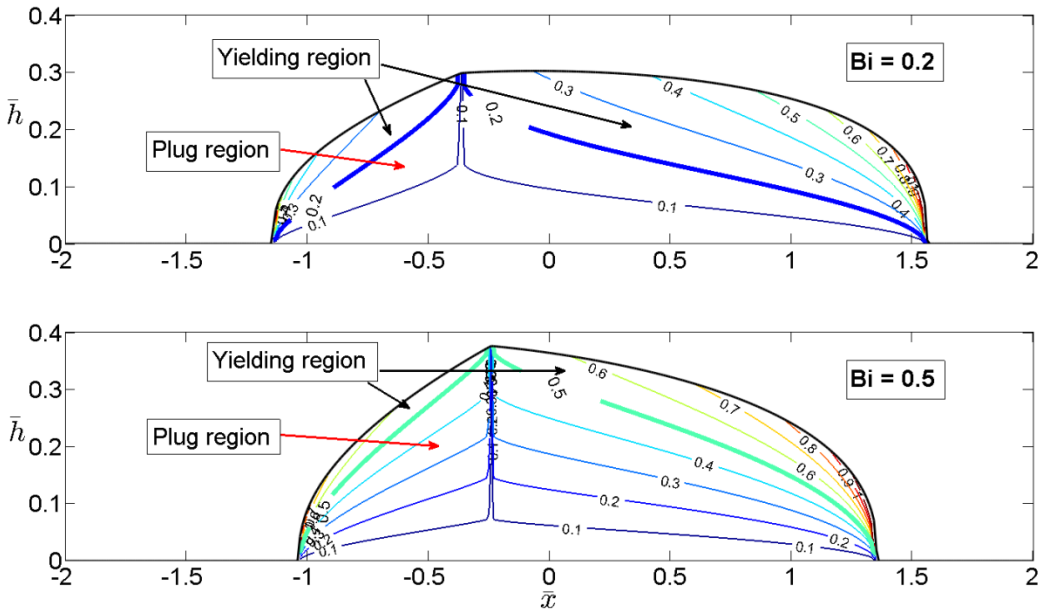

Figure 2.4. Dimensionless shear stress contours at $\bar{t}$ =10 for 2 different *Bi* ratio = 0.2 and 0.5. The value of *EG* = 10 and *n* =1 used for both simulations. The thick contour line indicates the yield surface below which we have the non-yielding plug layer.

2.3.1 Parametric Study in Dimensionless Form

In this section, a series of numerical simulations were carried out in dimension-less form as described in Equation 2.3, to investigate how the tissue elasticity and gel yield stress influence the coating mechanism. Numerical simulations were performed for EG = 1, 5, 15 and 25 to

investigate the effect of tissue elasticity. Using our non-dimensional scaling, EG = 1-25 corresponds to tissue elasticity of approximately 2-50 kPa. Results show that increasing the magnitude of tissue elasticity increases the extent of coating and also causes noticeable upward flow (Figure 2.2). At low values of EG, the flow is mostly downwards due to the influence of gravity. Effect of yield-stress on spreading was investigated by performing numerical simulations for Bi = 0, 0.2, 0.5 and 1. This range of Bi number corresponds to a dimensional yield-stress of approximately 0-30 Pa.

Results show that increasing the yield stress (or Bi ratio) decreases the extent of spreading (Figure 2.3) by reducing the yielding region of the flow domain. Figure 2.4 shows the shear stress contours at $\bar{t}$ = 10 for two different Bi values: 0.2 and 0.5. The thick contour line shows the yield surface which separates the yielding region from the plug flow region. The fluid is yielding in regions where the dimensionless shear stress is higher than the Bi value. As shown in Figure 2.4, the yielding region for Bi = 0.5 is much smaller than the yielding region for Bi = 0.2. We can easily calculate the percentage of the fluid domain that is yielding at any given time since we know the location of the yield surface and the fluid/solid interface. Figure 2.5 shows the influence of yield stress on the coating length and percentage yielding area over a period of time. The percentage yielding drops rapidly over time for the higher yield stress fluid and this behavior can be leveraged to improve the retention time of microbicidal gels.

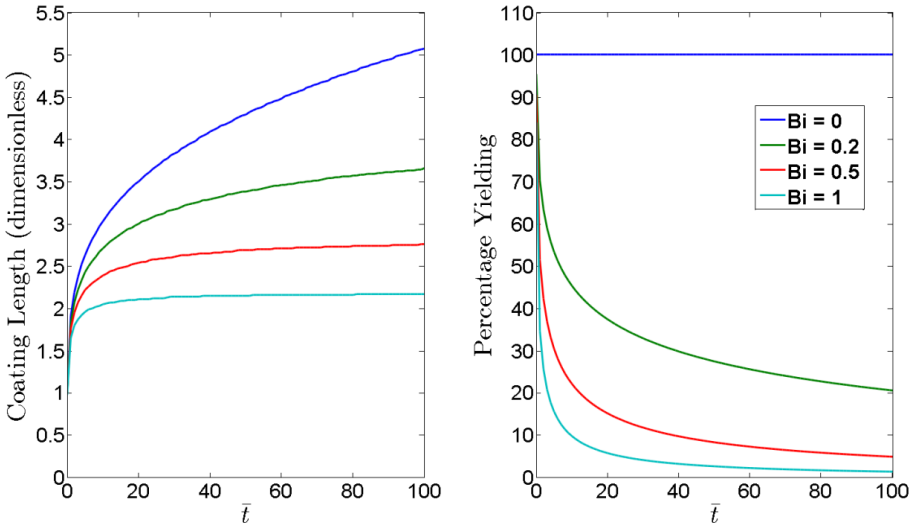

Figure 2.5. Effect of yield stress on coating length and the percentage yielding area of fluid over dimensionless time. The value of *EG* = 10 and *n* =1 used for all simulations. The yielding area was calculated by subtracting the plug area from the total fluid area and expressed as a percentage of the total area.

2.3.2 Gel Property Estimation for Optimal Coating Performance

Running a series of numerical simulations provides us useful insight about the transient coating behavior of gels for different tissue elasticity and rheological properties. However, we would also like to estimate the rheological properties required to achieve an optimal epithelial coverage and maximize retention. In particular, we would like to optimize delivery for a given tissue elasticity in a target deployment time. Mahalingam *et al.* used a response surface methodology, which is a visual technique, to design semi-solid microbicidal gels based on the squeezing flow model of gel spreading between rigid boundaries [50]. Our approach is to estimate the gel rheological properties such that it minimizes the percentage yielding at the end of a target deployment time while achieving the target epithelial coating for a given tissue elasticity.

The approach involves three analysis steps: (1) we performed a set of numerical flow simulations in dimensional form, (2) we developed nonlinear regression models for coating length and percentage yielding by fitting the output data from the numerical flow simulations, and (3) we solved the inverse problem for several cases. First, we created 500 quasi-random test points within our parameter ranges by using the *sobolset* function in Matlab®. We used the rheological property ranges mentioned previously (m = 10-80 Pa-s^n, n = 0.25-1.0 and τ_0 = 0-100 Pa) and a range of tissue elasticity E = 1-50 kPa for creating the model building set. These 500 parameter sets were inputs to the numerical simulation in dimensional form given by Equation 2.2. We considered a maximum deployment time of 180 seconds, relevant for the coitally-dependent drug delivery method where the user would insert the gel prior to the intercourse.

Second, we used nonlinear regression to fit the numerical results (for coating and % yielding) to the parameters $m, n, \tau_0, E \text{ and } t$. A regression model is needed for the subsequent step in mathematical optimization. We chose a regression model-based approach because, we were not optimizing the primary variable of the PDE ($h(x,t)$) and the nonlinear problem had many local optima. The resulting regression model for coating length and percentage yielding is given in Appendix A1. Several models containing various combination of the parameters were generated in the R© software. Model selection was based on Mallow's C_p statistic which indicates potential over-fitting of model with increasing number of parameters. The model with good coefficient of determination (*adjusted* R^2) and lowest Mallow's C_p was selected. A k-fold cross-validation (for k = 10) was performed to calculate the predictive squared correlation coefficient (Q^2). The calculated Q^2 of the proposed models were very close to R^2, which indicates that the models are adequate for predicting the spreading and percentage yielding of the injected gel bolus over time. The resulting statistical indicators are reported in Table 2.1.

Third, the above regression models were used to solve the inverse problem using a nonlinear optimization method in order to estimate the gel rheological properties (τ_0, m and n) that result in minimum percentage yielding and achieve the target coating length for a given tissue elasticity and deployment time. The optimization problem was formulated as follows:

$$minimize \quad \%\boldsymbol{Yielding}$$

$$\boldsymbol{s.t.}$$

$$Coating\ length \geq Target\ length$$

$$m_{min} \leq m \leq m_{max}$$

$$n_{min} \leq n \leq n_{max}$$

$$\tau_{0_{min}} \leq \tau_0 \leq \tau_{0_{max}}$$

$$E = Given\ tissue\ elasticity$$

$$t = Deployment\ time$$

The optimization problem was solved to local optimality by using the optimization software GAMS and applying the CONOPT nonlinear solver [51]. Table 2.2 provides an example list of estimated rheological properties for different tissue elasticity and deployment times. Two sets of feasible solutions are reported in the table to emphasize the possibility of multiple feasible solutions for nonlinear optimization problems. Solution of the problem that is obtained may vary depending on the initial guess. Moreover, the solver can be forced to find solutions within a specific range of a particular rheological parameter by enforcing a constraint on the maximum or minimum allowable limit. These estimations can provide microbicide designers with a specific set of target rheological properties which can be used to rationally design gels. Results in Table 2.2 show that the estimated m is reaching towards the lower limit of our model (10 Pa-s^n) when longer coating lengths at a relatively lower tissue elasticity are required. This indicates an important conclusion: a larger initial bolus volume is necessary if longer coating length (with maximized retention) is required for tissues with lower elasticity.

Table 2.1. Statistical indicators for regression models

Model name	Adjusted R^2	Q^2	p-value
Coating length	0.9745	0.9744	< 2.2e-16
% Yielding	0.9278	0.9275	< 2.2e-16

Table 2.2. Estimation of required rheological properties for achieving target coating and maximizing retention for specific tissue elasticity at a given time. Possibility of multiple feasible solutions are demonstrated here.

Target length (*cm*)	Tissue elasticity (*kPa*)	Deployment time (*sec*)	Estimated (m, n, τ_0) (*Pa-s^n, no unit, Pa*)	Estimated Spreading (cm)	Estimated % Yielding at the end of deployment time
7	15	150	(20.0, 0.9, 45.218)	7.00	1.038
			(27.0, 1.0, 43.671)	7.00	2.911
8	25	120	(25.0, 1.0, 46.554)	8.00	4.229
			(50.0, 0.95, 37.019)	8.00	16.505
9	20	150	(10.0, 1.0, 30.34)	9.00	8.489
			(20.0, 0.9, 25.539)	9.00	16.941
10	20	180	(10.0, 1.0, 19.468)	10.0	18.92
			(16.0, 0.95, 16.667)	10.0	24.574
	10		(10.0, 1.0, 2.514)	10.0	38.287

2.4 Conclusion

The study has presented a model framework which can be used to design gel formulations and delivery location (along the vaginal axis) for specific groups of women, whose vaginal tissue properties may vary with parameters such as age or parity. Importantly, it demonstrates a framework for optimizing more than one target behavior simultaneously – a method we can extend in the future to a larger set of target gel functions (e.g. biocompatibility or anti-STI activity). While using this type of regression model based optimization, it is always important to ensure that an appropriate range of rheological properties, tissue elasticity, deployment time and initial bolus volume is chosen for the model building set. Our model neglected the effect of boundary dilution. In the future, we would like to investigate whether boundary dilution has any significant effect within such a short time scale of deployment (2-5 minutes). The results of the presented numerical study will also enable us to investigate the effect of viscoelastic properties of the vaginal and surrounding tissue on the microbicidal flow dynamics. This model also assumes the tissue of the vaginal and surrounding structures to be homogeneous and isotropic which is not the case in reality. Future studies may incorporate layers of different tissues (e.g. vaginal epithelium, smooth musculature, and underlying tissues such as bladder structures) in the surrounding "tissue" compartment of the model. Therefore, it is crucial that efforts are made towards developing new instruments so that vaginal mechanical properties could be measured *in vivo,* and the impact of the surrounding underlying tissues on the closing pressures of the vaginal tissue could be quantified and modeled. These measured properties can then be used in numerical models to study the deployment dynamics more accurately.

Chapter 3

MATHEMATICAL MODELING OF RUPTURE AND DEWETTING OF ELLIS-TYPE SHEAR-THINNING LIQUID FILMS

3.1 Introduction

In thin films where surface tension plays an important role, a small perturbation of the interface shape can grow and eventually result in the rupture of the film. Rupture is the process where the film thickness approaches zero at a finite time point. The subsequent spatial growth of the minimum height, which forms dry spots in the liquid film is known as dewetting. Thin coating films are observed in many industrial and natural applications, such as microscale printing [33], industrial coatings [32], polymer solar cells [30], tear film [31], lung surfactant [29] etc. A microbicidal gel is another example of a barrier film, which is deployed at the lower female reproductive tract as a delivery vehicle of active pharmaceutical ingredients against HIV and other sexually transmitted infections, and it is also used to act as a physical barrier between the pathogens and the biological tissue. In most applications, it is desirable to avoid dry spots or uneven coating for both functional and aesthetic purposes.

Early theoretical works have predicted the rupture time and wavelength of the most unstable mode (preferred mode) of instability of thin films [17, 34]. The most unstable mode is

defined as the wavelength at which the initial disturbance grows most rapidly, and is the most likely initial spacing between mounds or ridges for a randomly imposed perturbation. However, a number of these studies used a simplified model of disjoining pressure (the dynamic pressure arising from solid/fluid interaction at molecular level) that allowed the model to represent the film evolution only up to the point of film rupture. Later works have used a more complex model of disjoining pressure that allowed the modeling of the dewetting process followed by rupture [35]. The growth rate of disturbance has been shown to be proportional to surface tension and the contact angle, and inversely proportional to the film thickness and viscosity in Newtonian fluids [35]. The wavelength of the most unstable mode (preferred mode) of instability has been shown to be proportional to the film thickness and inversely proportional to the contact angle [35]. Researcher have investigated the rupture/dewetting behaviors of evaporating films [17, 36], films with trapped nano-bubbles [37], and colloidal suspension [38]. Evaporation (condensation) leads to faster (slower) growth of initial disturbance [17]. Presence of nano-scale bubbles has also been shown to accelerate the rupture process [37]. Dewetting models of evaporating colloidal suspension has been developed to explain the self-pinning of receding contact line which is related to the formation of rings of dried particles, also known as the “coffee ring” effect [38]. Most of the above studies have considered a Newtonian fluid behavior. However, the rheological behavior of many industrial and biological fluid exhibit shear-thinning behavior. In this study, we use the Ellis rheological model which describes a shear-thinning fluid that has a low shear-rate Newtonian plateau.[39]

In this chapter, we present a mathematical model for the evolution of the rupture and dewetting process of Ellis-type shear-thinning liquid films. The goal of this chapter is to investigate the effect of shear-thinning on (a) the rupture time, and (b) the length-scale (wavelength) of the most unstable (preferred) mode of instability.

3.2 Problem Formulation

We consider a thin layer of liquid film or droplet on a plane substrate. The thickness of the liquid film is represented in dimensional form by $\bar{h}(\bar{x},\bar{y},\bar{t})$ where $\bar{x}$ and $\bar{y}$ axes are orthogonal on the plane of the substrate, and $\bar{t}$ is the time. We assume an Ellis constitutive model for describing the shear-thinning behavior of the thin film [39]:

$$\frac{1}{\bar{\eta}} = \frac{1}{\bar{\eta}_0}\left(1+\left|\frac{\tau}{\tau_{1/2}}\right|^{\lambda-1}\right) \tag{3.1}$$

Here, $\bar{\eta}$ is the viscosity, $\bar{\eta}_0$ is the viscosity at zero shear stress, $\tau_{1/2}$ is the shear-stress at which the viscosity is reduced by half, and λ is the shear-thinning index. When λ = 1, the liquid is Newtonian, while for λ > 1, the liquid is shear-thinning. At a high shear stress, the Ellis model exhibits power-law type shear-thinning behavior. However, the Ellis model has a low shear stress Newtonian plateau. Since high shear stresses only occur near the contact line, the Ellis model is a particularly interesting candidate for modeling thin film flows of shear-thinning liquid films because it can capture the Newtonian behavior in the low shear-rate regions.

Assuming slow flow and, and small slope approximation of the free surface curvature to the Navier-Stokes equations (the thin film “lubrication approximation”), and considering an incompressible liquid, a partial differential equation for the film thickness evolution equation can be derived. Applying a no-slip boundary condition at the substrate and assuming zero stress at the air-liquid interface, we arrive at the 3D thin film (i.e. 2D spreading) equation:

$$\frac{\partial \bar{h}}{\partial \bar{t}} = -\nabla \bullet \bar{Q} = -\frac{1}{3\eta_0}\left(\frac{\partial \bar{Q}_x}{\partial \bar{x}} + \frac{\partial \bar{Q}_y}{\partial \bar{y}}\right) \tag{3.2}$$

$$\overline{Q}_x = \overline{h}^3 \frac{\partial}{\partial \overline{x}} \left(\sigma \nabla^2 \overline{h} + \overline{\Pi} \right) \overline{F}$$

$$\overline{Q}_y = \overline{h}^3 \frac{\partial}{\partial \overline{y}} \left(\sigma \nabla^2 \overline{h} + \overline{\Pi} \right) \overline{F}$$

$$\overline{F} = 1 + \frac{3}{\lambda + 2} \left(\frac{\overline{h}}{\tau_{1/2}} \right)^{\lambda - 1} \left(\left[\frac{\partial}{\partial \overline{x}} \left(\sigma \nabla^2 \overline{h} + \overline{\Pi} \right) \right]^2 + \left[\frac{\partial}{\partial \overline{y}} \left(\sigma \nabla^2 \overline{h} + \overline{\Pi} \right) \right]^2 \right)^{\frac{\lambda - 1}{2}}$$

Here, σ is the surface tension, and $\nabla^2 \overline{h}$ is the small slope approximation of the free surface curvature. See Appendix A3 for details of the derivation. The term $\overline{\Pi}$ is known as the disjoining pressure. The simplest model for disjoining pressure is given by

$$\overline{\Pi} = \frac{A}{\overline{h}^3} \tag{3.3}$$

Here, A is a van der Waals attraction force between two surfaces, known as the Hamaker constant [52]. This model of disjoining pressure was used by many researchers to study the finite-time rupture of thin liquid films [17, 34, 37, 53]. However, a problem with this model is that it cannot be continued past the time of first occurrence of film rupture because the thickness becomes negative. This problem can be avoided by considering a more detailed model for disjoining pressure, so that the dewetting process can also be simulated. In this study, we use the two term disjoining pressure model introduced by Frumkin [54] and Derjaguin [55]:

$$\overline{\Pi} = \overline{C} \left[\left(\frac{\overline{h}_*}{\overline{h}} \right)^n - \left(\frac{\overline{h}_*}{\overline{h}} \right)^m \right] \tag{3.4}$$

Here, $\bar{C}$, and the exponents n and m are positive constants with $n > m > 1$. The local disjoining energy density has a single stable energy minimum at the thin precursor layer thickness, $\bar{h} = \bar{h}_*$. When the thickness of the film reaches that of the precursor layer, the disjoining pressure within the precursor layer exactly balances the capillary pressure. Since the disjoining pressure is assumed to depend on only the local interfacial separation $\bar{h}$, the validity of the expression in Equation 3.4 also requires small slope approximation. The thickness of the precursor layer is generally small compared to the thickness of the film, and it allows the motion of the apparent contact line by removing the shear-stress singularity. The exponents (n, m) are selected to $(3,2)$ following previously published literature [35]. The term $\bar{C}$ is given by (see reference [35, 56] for details):

$$\bar{C} = \frac{(n-1)(m-1)}{\bar{h}_*(n-m)}\sigma(1-\cos\theta_e) \approx \frac{(n-1)(m-1)}{2\bar{h}_*(n-m)}\sigma\theta_e^2 \tag{3.5}$$

Here, θ_e is the equilibrium contact angle. The wettability is controlled by the constant, $\bar{C}$. Small or zero value of the constant indicates good or perfect wetting conditions, whereas higher values indicate partial wetting scenarios.

The dimensionless formulation is developed by considering appropriate scales following reference [35]. Using initial film thickness, h_0, characteristic length scale of l_c on the substrate plane, and zero shear rate viscosity η_0 as reference quantities, the transformation to dimensionless variables are

$$h = \bar{h}/h_0, x = \bar{x}/l_c, y = \bar{y}/l_c, t = \bar{t}/t_c \tag{3.6}$$

The characteristic time is given by

$$t_c = \frac{3\eta_0 {l_c}^4}{\sigma {h_0}^3} \tag{3.7}$$

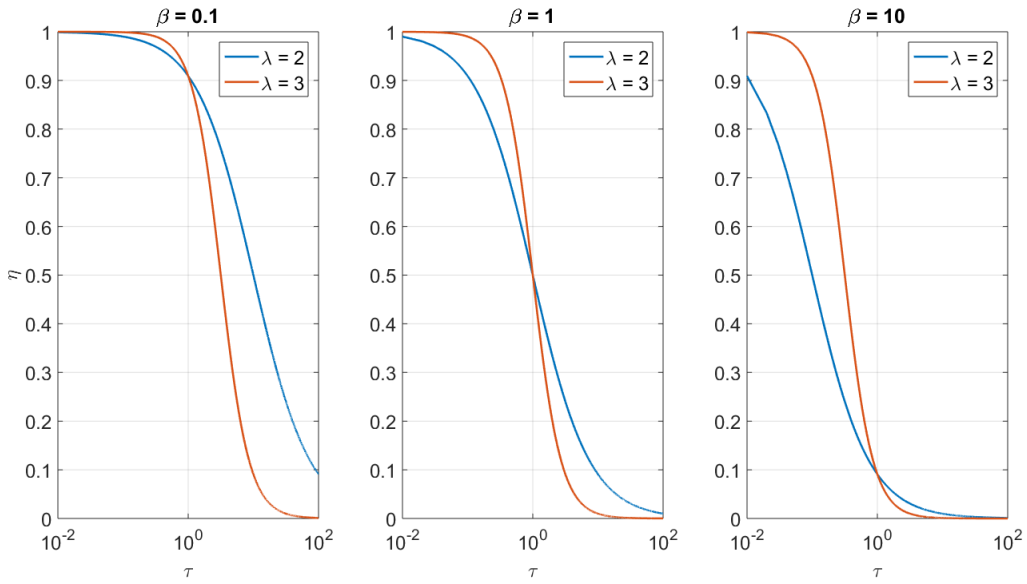

Figure 3.1. Example plot of dimensionless viscosity as a function of shear stress for Ellis fluid

Following Braun *et al*. [57], the non-dimensional form of Ellis model can be written as:

$$\eta = \frac{1}{1+\beta|\tau|^{\lambda-1}} \tag{3.8}$$

Here, $\beta = \left(\left(\sigma {h_0}^2/{l_c}^3\right)/\tau_{1/2}\right)^{\lambda-1}$ describes the degree of shear-thinning. A value of $\beta = 0$ returns a Newtonian fluid behavior whereas increasing value of β indicates increased shear-thinning. The other shear-thinning parameter λ determines the slope of the power-law type shear-thinning region. Higher value of λ indicates a broader Newtonian plateau. Therefore, fluids with higher value of λ will act more Newtonian-like at low shear stresses. Figure 3.1 shows behavior of Ellis fluid as a function of shear stress.

The 3D dimensionless evolution equation (2D PDE), with these scaling becomes:

$$\frac{\partial h}{\partial t} = -\frac{\partial Q_x}{\partial x} - \frac{\partial Q_y}{\partial y} \tag{3.9}$$

$$Q_x = h^3 \frac{\partial}{\partial x}\left(\nabla^2 h + \Pi\right) F$$

$$Q_y = h^3 \frac{\partial}{\partial y}\left(\nabla^2 h + \Pi\right) F$$

$$F = 1 + \frac{3\beta}{\lambda + 2} h^{\lambda - 1}\left(\left[\frac{\partial}{\partial x}\left(\nabla^2 h + \Pi\right)\right]^2 + \left[\frac{\partial}{\partial y}\left(\nabla^2 h + \Pi\right)\right]^2\right)^{\frac{\lambda-1}{2}}$$

$$\Pi = C\left[\left(\frac{h_*}{h}\right)^n - \left(\frac{h_*}{h}\right)^m\right]$$

$$C = \frac{(n-1)(m-1) l_c{}^2 \theta_e{}^2}{2h_*(n-m) h_0{}^2}$$

Here, C is the dimensionless contact angle parameter that defines the wettability. We first perform a rupture and dewetting study in 2D (1D PDE) (a) to evaluate the rupture time of shear-thinning fluids compared to Newtonian fluids, and (b) to evaluate the effect of perturbation wavelength on the rupture time. The 2D evolution equation is given by

$$\frac{\partial h}{\partial t} + \frac{\partial}{\partial x}\left[h^3 \frac{\partial}{\partial x}\left(\frac{\partial^2 h}{\partial x^2} + \Pi\right) F\right] = 0 \tag{3.10}$$

$$F = 1 + \frac{3\beta}{\lambda + 2} h^{\lambda - 1} \left(\left[\frac{\partial}{\partial x} \left(\frac{\partial^2 h}{\partial x^2} + \Pi \right) \right]^2 \right)^{\frac{\lambda - 1}{2}}$$

For the 2D numerical simulation, we use an initial condition in the form $h(x,0) = 1 - 0.1\cos(\pi x / L)$, where L is the length of the domain. Periodic boundary condition is enforced at the two ends of the domain. We investigated the effect of shear-thinning by performing numerical simulations with β = 0.1, 1, 10 and λ = 2, 3. We have compared the scaled rupture time with that of the Newtonian fluid to investigate the influence of shear-thinning on unstable film rupture. Figure 3.2 shows a schematic of the form of the initial sinusoidal perturbation. For the 3D simulation, we use an initial condition in the form $h(x, y, 0) = 1 + h_1(x, y)$, where h_1 is a random number between -0.01 and 0.01. Periodic boundary conditions were enforced at the domain boundaries. The simulation was performed in a domain of $(L_x \times L_y) = (50 \times 50)$.

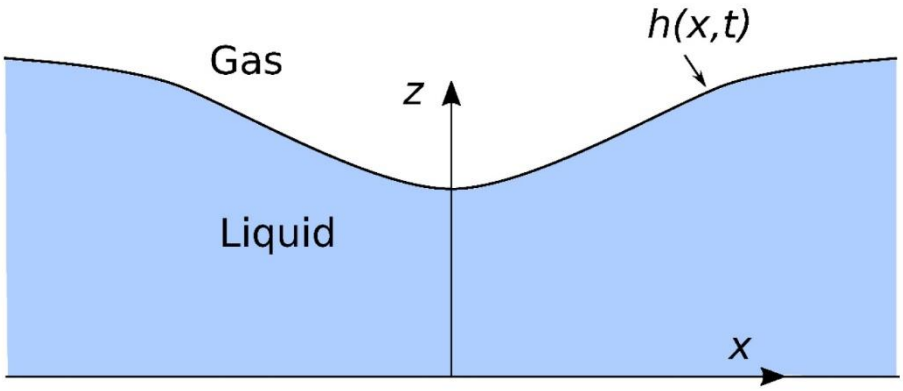

Figure 3.2. Schematic of a sinusoidal initial perturbation of the interface of a thin liquid film on a solid substrate.

All simulations were performed for precursor layer thickness, $h_*/h_0 = 0.1$. Second order central difference scheme was used to discretize the spatial variables and time integration was

performed using Matlab's variable step ODE15s solver with default tolerance of 1E-6. Volume of the fluid was monitored as a function of time since insufficient spatial or temporal resolution would violate the conservation of mass.

3.3 Results and Discussion

For partially wetting fluid, a value for the contact angle parameter C needs to be selected which can be used in the model. A linear stability analysis performed by Schwartz *et al*. predicted a relationship between the most unstable wavenumber and the contact angle parameter by the following expression for a Newtonian fluid (see [35] for details):

$$q_{\max}^{\ 2} = \frac{mCh_*^{\ m}}{2h_0^{\ m+1}} \tag{3.10}$$

Here, q_{max} is the most unstable wavenumber, which is related to the wavelength, L by the expression, $q_{max} = 2\pi/L$. Using a q_{max} value of 0.707, which is obtained from linear stability analysis performed for Newtonian fluids by several authors [17, 37, 58] for the simple disjoining pressure model as described in Equation 3.3, we obtain $C \approx 50$.

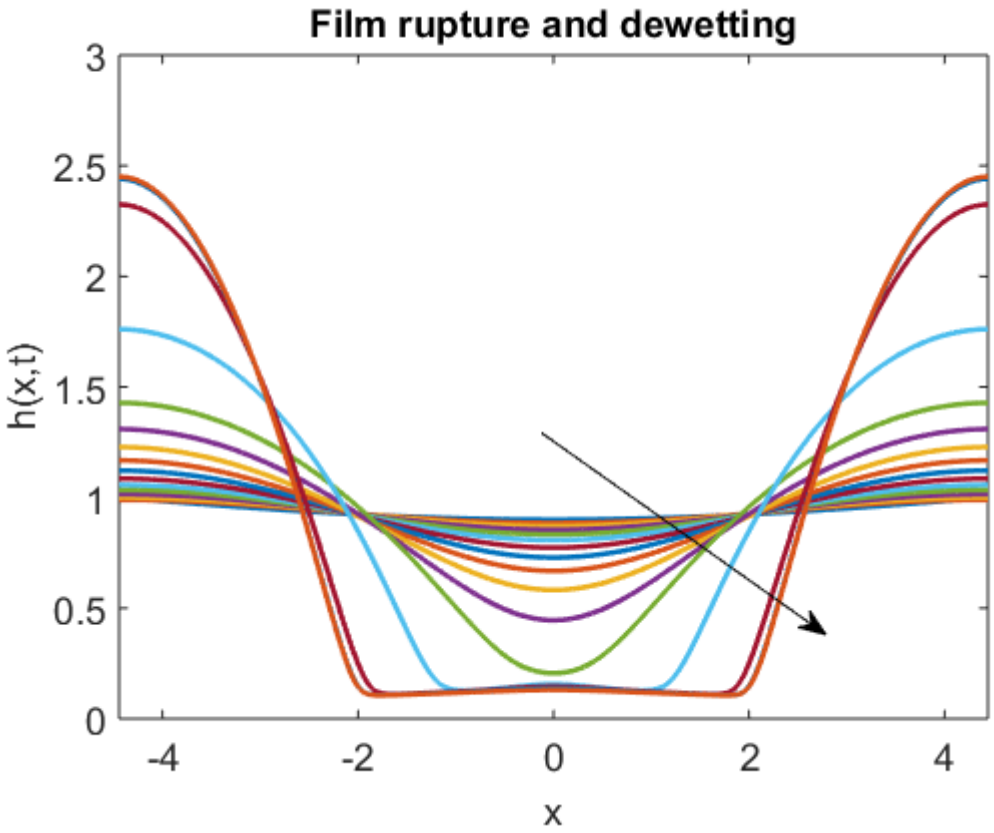

Figure 3.3. Example of a numerical simulation of the rupture and dewetting process of a Newtonian thin film. Rupture is defined as the point where the film thickness reaches that of the precursor layer thickness, and dewetting is the process of subsequent hole growth. The plot shows several snapshots of the film profile as a function of time. Simulation was performed on a grid with $\Delta x = 0.01$.

3.3.1 2D simulation

Figure 3.3 shows a representative illustration of the rupture and dewetting process for a Newtonian thin film. As mentioned earlier, the selection of Deraguin disjoining pressure model allows us to continue the simulation after the rupture point (where the film thickness reaches that of the precursor layer thickness).

Figure 3.4 shows the effect of wavelength on the rupture time for Newtonian and Ellis-type thin films. The rupture point was considered as the time when the film thickness reaches within 10% of the precursor layer thickness. It can be seen that increasing the value of β (i.e. increasing shear-thinning) reduces the rupture time. No significant change in the most unstable wavelength is observed from the simulations. However, cases with $\lambda = 2$ displays a much faster rupture process compared to that of $\lambda = 3$, for all cases of β. This is because of the narrower Newtonian plateau in the prior case. At low shear stresses, smaller values of λ acts more shear-thinning.

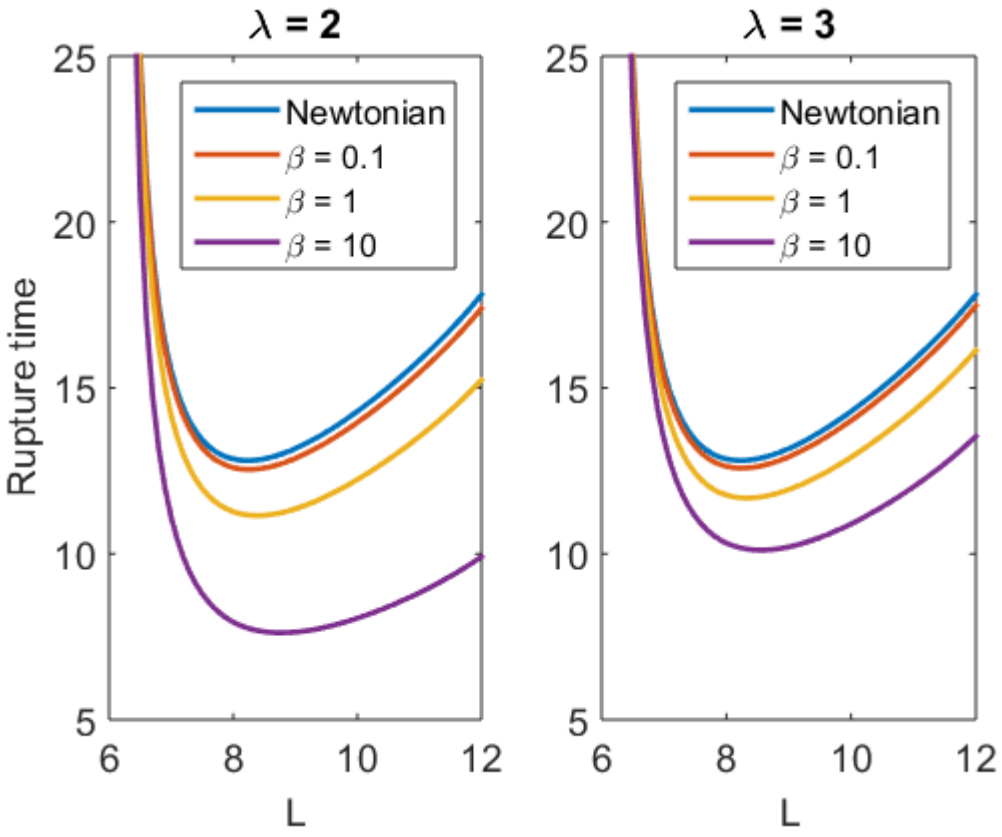

Figure 3.4. The rupture time versus wavelength for Newtonian and different cases of Ellis-type shear thinning fluid. Shear-thinning has negligible effect on the preferred mode of instability. The grid size for simulation was $\Delta x = 0.01$.

Figure 3.5 shows the rupture process by plotting the scaled minimum film thickness as a function of time for a specific wavelength, $L = 8.887$ (wavenumber, $q = 0.707$). The results demonstrate how the shear-thinning behavior accelerates the rupture process, which is defined as the film thickness reducing to that of the precursor layer thickness. The early time film thickness evolution are very similar for both Newtonian and shear-thinning fluids. However, the thickness evolution of shear thinning fluid quickly accelerates due to the decrease in the apparent viscosity. As mentioned earlier, a narrower Newtonian plateau (i.e., the smaller λ) leads to faster rupture of the thin film.

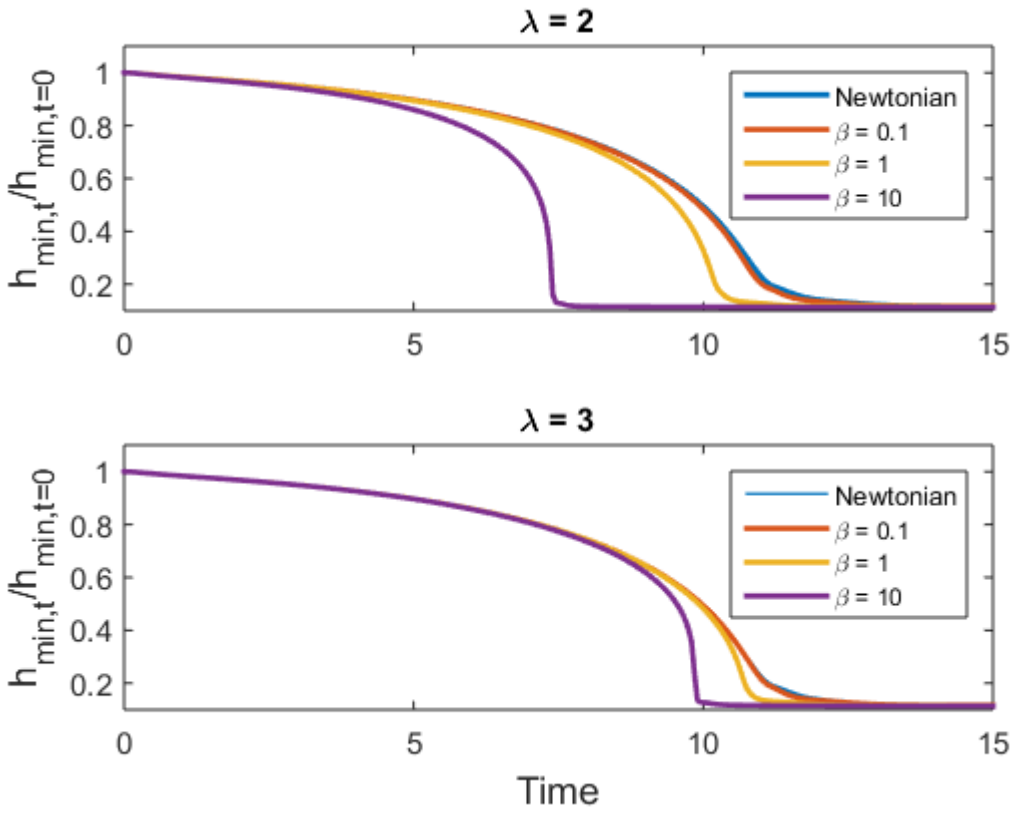

Figure 3.5. Comparison of rupture process for Newtonian and Ellis-type shear-thinning fluid. Shear-thinning accelerates the rupture process. The grid size for simulation was $\Delta x = 0.01$.

3.3.2 3D Simulation

Figure 3.6 demonstrates an example of the rupture and subsequent dewetting process of thin films via several snapshots at different times after an initial disturbance in the scale of 1% of the film thickness is imposed. The results were consistent with the 2D simulation as it showed an acceleration of the rupture process due to the shear-thinning. As expected, the Newtonian thin film shows the slowest rupture/dewetting process, and the shear-thinning film with $\lambda = 2$ showed a faster rupture/dewetting compare to $\lambda = 3$. The initial spacing between the resulting ridges are qualitatively similar which was expected since shear-thinning did not make any significant change in the most unstable wavelength in our 2D simulations. Figure 3.7 plots the minimum film thickness from the 3D simulations. The behavior of film thickness evolution due to the random perturbation is consistent with the pattern observed in the 2D simulations where a single mode perturbation was applied to the initial film thickness. As discusses earlier, narrower Newtonian plateau (smaller λ) led to faster rupture of the thin film for the same value of $\beta = 10$.

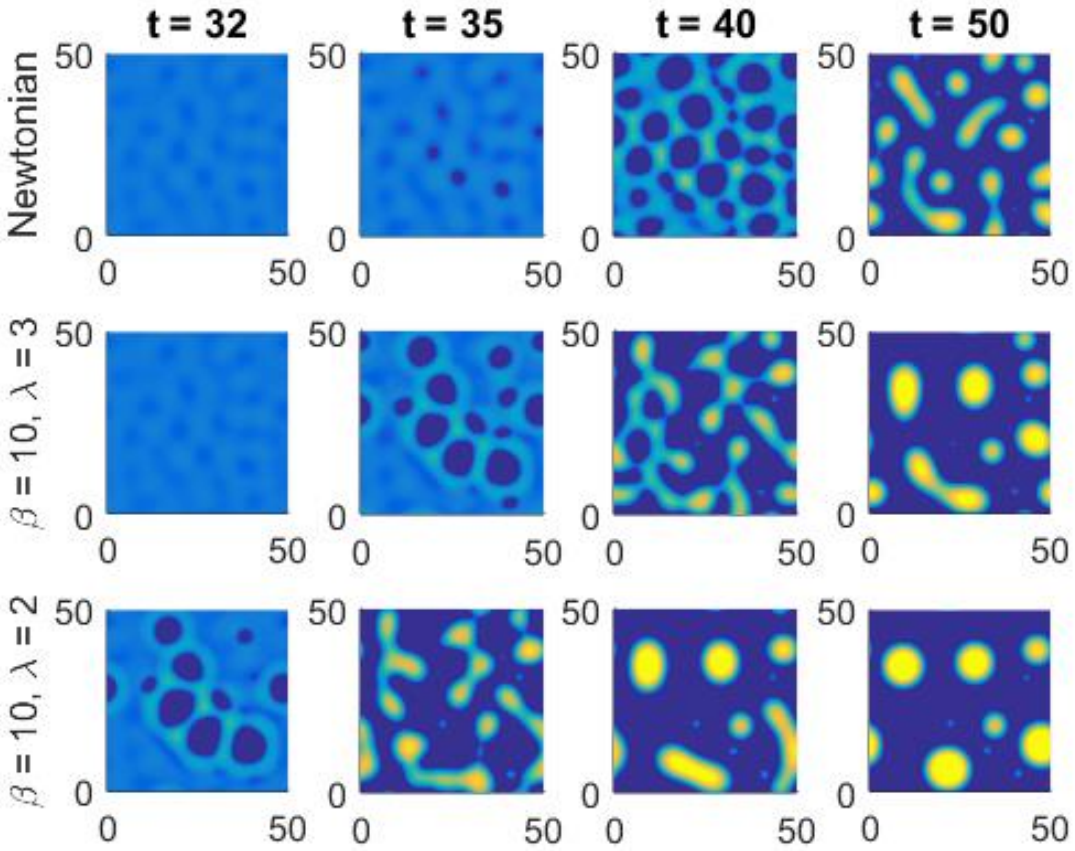

Figure 3.6. Example of 3D rupture and dewetting process of Newtonian and Ellis-type thin films via snapshots at different times. Simulation was performed in a domain of $(L_x \times L_y) = (50 \times 50)$ with grid size $\Delta x = 0.25$ and $\Delta y = 0.25$.

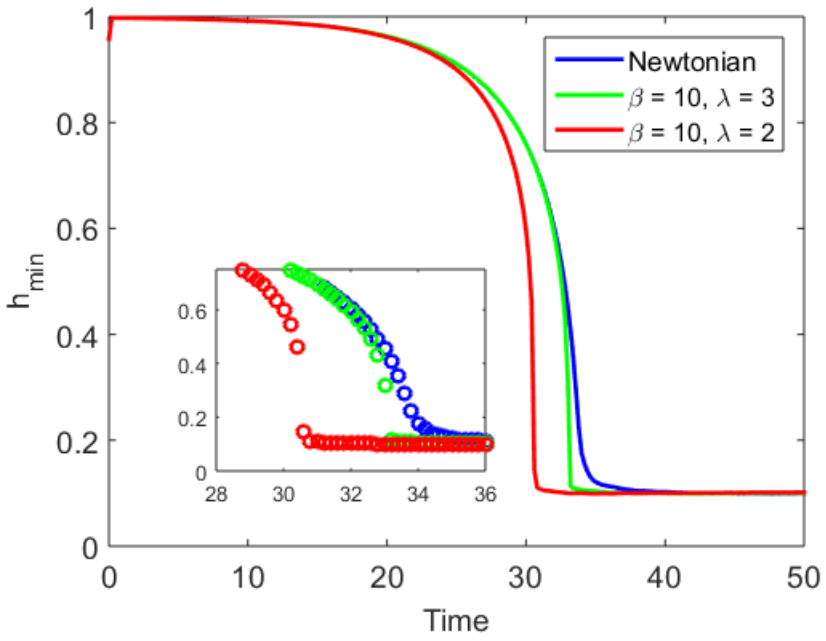

Figure 3.7. Minimum film thickness as a function of time from the 3D simulation.

3.4 Conclusion

In conclusion, we have developed a mathematical model of thin film evolution for Ellis-type shear-thinning fluid. We have neglected the effect of gravity and considered partial wetting. Substrate heterogeneity was not considered. Results of rupture/dewetting simulations of Ellis-type shear-thinning fluid have indicated that shear-thinning rheology increases the growth rate of instability but has a negligible effect on the wavelength of preferred mode of instability. However, the initial conditions in many industrial process (for example in roll to roll type coating process) might be significantly different. The shearing of the liquid in the processing equipment may reduce the apparent viscosity of the liquid prior to the application of coating, and the apparent viscosity

might go up significantly after the application of coating, which can help in slowing down of dewetting process, if a liquid with high zero shear rate viscosity is used. Experimental investigation of the dewetting process could be used to validate the finding of this numerical study, following the experimental procedures described in reference [35]. Future study could include Herschel-Bulkley type rheological model to study the effect of yield stress on the rupture and dewetting. Yield stress has been shown to suppress fingering instability in gravity-driven film flow [44]. A similar stabilizing effect in the case of free surface instability could potentially be achieved by using yield stress type fluids in micro-printing and coating applications.

Chapter 4

MATHEMATICAL MODELING OF CONTACT LINE INSTABILITY OF GRAVITY-DRIVEN FLOW OF ELLIS-TYPE SHEAR-THINNING LIQUID FILMS

4.1 Introduction

Gravity-driven thin film flow of viscous liquids on solid substrates have been extensively studied due to its ubiquitous presence in various fields such as paint/coating flows [59, 60], geological flows [11, 12], and microbicidal drug delivery [4-6, 23, 61]. Formation of finger-like patterns in thin films with a moving contact line is a well observed phenomena [18]. Contact line instability or 'fingering instability' which causes the formation of fingers downstream has been widely studied for Newtonian fluids by various researchers [16, 40, 41, 43]. Random perturbation at the contact line can cause the moving front to corrugate, and this behavior is a function of both the surface tension and inclination angle [43]. Driven thin films flowing on a substrate form a thick leading edge at the advancing contact line due to the action of the surface tension. This thick leading edge, also known as the 'capillary ridge' [1], is unstable to perturbations which are parallel to the advancing contact line [62]. Formation of fingers at the moving front is undesirable since it may lower the quality of coating, or negatively affect the barrier properties by leaving dry spots.

Huppert experimentally demonstrated the finger formation phenomena of thin films flowing down on an incline [18], which was followed by numerous experimental and numerical studies. Troian *et al.* performed linear stability analysis of thin film flow down a vertical plane and computed the wavelength that produces maximum growth rate of fingers [62]. Bertozzi and Brenner explained the discrepancies between linear stability analysis, and experimentally observed instability [16]. They have pointed out that transient amplification of small disturbances can occur in cases even when the linear stability analysis results indicate stability, and if the transient amplification is large enough to shift the system into a nonlinear regime, it can lead to instability. Kondic and Diez pointed out that flatter inclines decrease the growth rate of the disturbance, and makes the most unstable wavelength larger [42]. All the above studies were performed with a complete wetting assumption. Eres *et al*. studied instability of partial wetting thin films [63]. They have concluded that sufficiently large contact angle creates long straight sided fingers, and for even higher contact angle the fingers break up into a series of droplets.

Most of the work reported on contact line fingering instability have dealt with Newtonian fluids. However, non-Newtonian fluids are encountered in many industrial, biological and geophysical scenarios. There has been some published research regarding contact line fingering instability of non-Newtonian fluids in recent years. Balmforth *et al*. performed linear stability analysis of viscoplastic fluids, and their results indicated that yield stress can suppress the formation of fingers [44]. Numerical and experimental study on viscoelastic fluids have indicated that elasticity also tends to have a stabilizing effect [64, 65]. Shear-thinning has been shown to affect the size of the capillary ridge for power-law thin films, indicating that shear-thinning may also suppress fingering instability [1]. Our group had already performed numerical investigation on the effect of power-law rheology on contact line instability, and the results showed that shear-thinning indeed suppressed fingering instability [45]. However, the power-law model predicts an infinite viscosity at low shear rates whereas most real shear-thinning fluids have a low shear rate

Newtonian plateau [39]. This behavior may have an impact on the contact line instability. Therefore, we have chosen to subsequently study the contact line instability phenomena using the Ellis fluid model which has a more robust representation of shear-thinning behavior over a wider range of shear rates through the inclusion of a low shear rate Newtonian plateau.

In this chapter, we examine the stability of the contact line of an Ellis-type shear-thinning thin film. The approach is linear stability analysis (LSA), and verification by comparing the findings of LSA with the 3D nonlinear simulation of finger growth due to single mode and random multimode perturbations. This approach has been successfully applied in our previous study of power-law fluids [45].

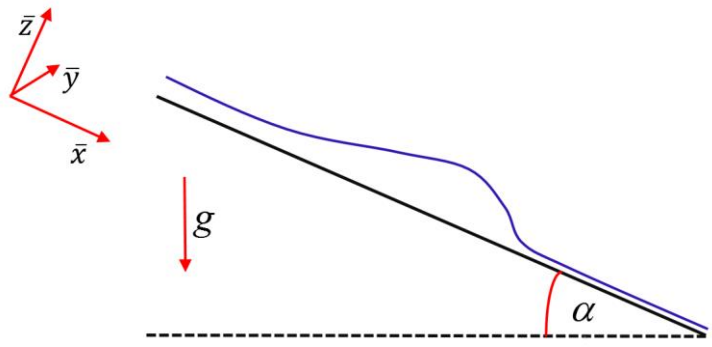

Figure 4.1. Schematic of the cross section of a thin film flowing down an incline due to the action of gravity.

4.2 Problem Formulation

We consider a thin film of viscous liquid flowing down on a solid substrate inclined at an angle α with the horizontal direction. Standard Cartesian coordinate system is considered where $\bar{x}$ is the direction of flow, $\bar{y}$ is the transverse direction and $\bar{z}$ is normal to the substrate. The liquid

surface corresponds to $\bar{z} = \bar{h}(\bar{x}, \bar{y}, \bar{t})$ where $\bar{t}$ is the time. We assume an Ellis constitutive model for describing the shear-thinning behavior of the thin film [39]:

$$\frac{1}{\bar{\eta}} = \frac{1}{\bar{\eta}_0}\left(1 + \left|\frac{\tau}{\tau_{1/2}}\right|^{\lambda-1}\right) \tag{4.1}$$

Here, $\bar{\eta}$ is the viscosity, $\bar{\eta}_0$ is the viscosity at zero shear stress, $\tau_{1/2}$ is the shear-stress at which the viscosity is reduced by half, and λ is the shear-thinning index. When λ = 1, the liquid is Newtonian, while for λ > 1, the liquid is shear-thinning. At a high shear stress, the Ellis model exhibits power-law type shear-thinning. However, the Ellis model has a low shear stress Newtonian plateau. Ellis model is a particularly interesting candidate for modeling thin film flows of shear-thinning liquid films because the free surface of thin film flows are stress free, and shear stress is small in regions that are far from the contact line.

We utilize the lubrication theory by depth averaging the liquid velocity over the thickness of the film. The governing differential equation describing the 3D flow (i.e. 2D spreading) of an Ellis thin film on an incline is given by:

$$\frac{\partial \bar{h}}{\partial \bar{t}} = -\nabla \bullet \bar{Q} = -\frac{1}{3\eta_0}\left(\frac{\partial \bar{Q}_x}{\partial \bar{x}} + \frac{\partial \bar{Q}_y}{\partial \bar{y}}\right) \tag{4.2}$$

$$\bar{Q}_x = \bar{h}^3\left[\rho g \sin\alpha - \rho g \cos\alpha \frac{\partial \bar{h}}{\partial \bar{x}} + \sigma \frac{\partial}{\partial \bar{x}}\left(\nabla^2 \bar{h}\right)\right]\bar{F}$$

$$\bar{Q}_y = \bar{h}^3\left[-\rho g \cos\alpha \frac{\partial \bar{h}}{\partial \bar{y}} + \sigma \frac{\partial}{\partial \bar{y}}\left(\nabla^2 \bar{h}\right)\right]\bar{F}$$

$$\bar{F} = 1 + \frac{3}{\lambda + 2}\left(\frac{\bar{h}}{\tau_{1/2}}\right)^{\lambda-1}\left(\left[\rho g \alpha \sin\alpha - \rho g \cos\alpha \frac{\partial \bar{h}}{\partial \bar{x}} + \sigma \frac{\partial}{\partial \bar{x}}\left(\nabla^2 \bar{h}\right)\right]^2 + \left[-\rho g \cos\alpha \frac{\partial \bar{h}}{\partial \bar{y}} + \sigma \frac{\partial}{\partial \bar{y}}\left(\nabla^2 \bar{h}\right)\right]^2\right)^{\frac{\lambda-1}{2}}$$

Here $[Q_x, Q_y]$ are mass flux, ρ is the viscosity, g is the acceleration due to the gravity, σ is the surface tension, and $\nabla^2 \bar{h}$ is the small slope approximation of the free surface curvature. See Appendix A4 for details of the derivation. For developing the non-dimensional form of the thin film evolution equation, the fluid height, $\bar{h}$ is scaled by the thickness of the film far behind the contact line, h_c. The spatial coordinates, and time are scaled as $(x, y, t) = (\bar{x}/x_c, \bar{y}/x_c, \bar{t}/t_c)$. Following Kondic [43], the characteristic spatial and time scale has been chosen to be:

$$x_c = \left(\frac{a^2 h_c}{\sin\alpha}\right)^{1/3} \tag{4.3}$$

$$t_c = \frac{3\eta}{\sigma}\frac{a^2 h_c}{h_c^2 \sin\alpha}$$

Here, $a = \sqrt{\sigma/\rho g}$ is known as the capillary length which provides a measure of the length scales when capillary effects become important compared to gravitational ones. The velocity scale is chosen as $U = x_c/t_c$. The capillary number is defined as $Ca = \eta U/\sigma$, which measures the relative importance of viscous forces to surface tension forces. Following Braun *et al*. [57], the non-dimensional form of Ellis model can be written as:

$$\eta = \frac{1}{1 + \beta|\tau|^{\lambda-1}} \tag{4.4}$$

Here, $\beta = \left(\rho g h_c \sin\alpha/\tau_{1/2}\right)^{\lambda-1}$ describes the degree of shear-thinning. A value of $\beta = 0$ returns a Newtonian fluid behavior whereas increasing value of β indicates increased shear-thinning. The other shear-thinning parameter λ determines the slope of the power-law type shear-thinning region. Higher value of λ indicates a Newtonian plateau over a wider range of shear stress. Therefore, fluids with higher value of λ will act more Newtonian-like at low shear stresses. Figure 4.2 shows behavior of Ellis fluid as a function of the shear stress.

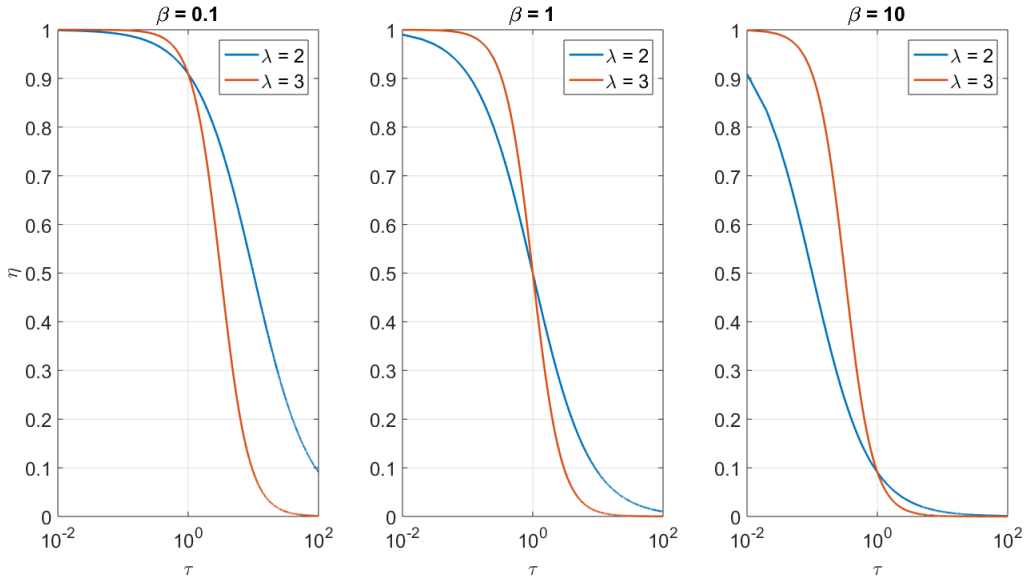

Figure 4.2. Plot of dimensionless viscosity as a function of dimensionless shear stress for Ellis fluid

With these rescaling, the non-dimensional evolution equation is described as:

$$\frac{\partial h}{\partial t} = -\frac{\partial Q_x}{\partial x} - \frac{\partial Q_y}{\partial y} \tag{4.5}$$

$$Q_x = h^3\left(1 - Dh_x + \left(\nabla^2 h\right)_x\right)F$$

$$Q_y = h^3\left(-Dh_y + \left(\nabla^2 h\right)_y\right)F$$

$$F = 1 + \frac{3\beta}{\lambda+2}h^{\lambda-1}\left[\left(1 - Dh_x + \left(\nabla^2 h\right)_x\right)^2 + \left(-Dh_y + \left(\nabla^2 h\right)_y\right)^2\right]^{\frac{\lambda-1}{2}}$$

Here, $D = (3Ca)^{1/3}\cot\alpha$ is the measure of normal component of gravity ($D = 0$ indicating vertical incline whereas larger D indicating flatter inclines) [16, 43]. All the analysis were performed by considering a completely wetting fluid with zero equilibrium contact angle, and adopting a precursor film of thickness b to alleviate the contact line singularity [40, 66]. A decrease in the value of b increases the growth rate of disturbance due to the increased height of the capillary ridge [16]. We have used $b = 0.1$, following published literature on Newtonian [43] and power-law [45] thin film models.

4.2.1 Travelling Waves and Linear Stability Analysis

To perform linear stability analysis, a travelling wave solution was first determined as a base state. Detailed description of techniques used for obtaining travelling wave solutions, and linear stability analysis has been reported in previous literatures [16, 43]. The base state before the onset of instability is a travelling wave solution $h(x, y, t) = h_0(x - Ut)$ of equation (4.5). The function $h_0(x)$ satisfies the following equation.

$$-Uh_0 + h_0^3\left(1 - Dh_{0x} + h_{0xxx}\right)\left(1 + \frac{3\beta}{\lambda+2}h^{\lambda-1}\left[\left(1 - Dh_{0x} + h_{0xxx}\right)^2\right]^{\frac{\lambda-1}{2}}\right) = f \qquad (4.6)$$

Here, the moving reference frame velocity, U, and the constant of integration, f, can be found by matching the front onto the rest of the solution: $x \to -\infty, h_0 \to 1$ and $x \to \infty, h_0 \to b$, where $b = 0.1$

is the thickness of the precursor layer. Using these two matching conditions, we get the following travelling wave velocity and integration constant.

$$U = \frac{1-b^3}{1-b} + \frac{3\beta}{\lambda+2}\frac{1-b^{\lambda+2}}{1-b} \tag{4.7}$$

$$f = -\frac{1-b^3}{1-b} + \frac{3\beta}{\lambda+2}\left(1-\frac{1-b^{\lambda+2}}{1-b}\right)$$

The y independent PDE governing the shape of the front can be written as:

$$\frac{\partial h}{\partial t} = -\frac{\partial}{\partial x}\left[h^3\left(1-Dh_x+h_{xxx}\right)\left(1+\frac{3\beta}{\lambda+2}h^{\lambda-1}\left[\left(1-Dh_x+h_{xxx}\right)^2\right]^{\frac{\lambda-1}{2}}\right)\right]+U\frac{\partial h}{\partial x} \tag{4.8}$$

The base profile can be obtained by either solving the ODE in equation 4.6, or the PDE in Equation 4.8. We have solved Equation 4.8 numerically to get the base state profile. Once the base state solution, $h_0(x)$ is achieved, we consider a perturbation, $\varepsilon h_1(x,y,t)$ to the front h_0. Here, h_0 and h_1 are of $\mathcal{O}(1)$, and $\varepsilon \ll 1$. We plug in $h(x,y,t) = h_0(x) + \varepsilon h_1(x,y,t)$ into the 3D non-dimensional PDE in the moving reference frame, and linearize the PDE by keeping only the terms that are in the order of ε. Next, we replace the solution h_1 by its Fourier integral in y by using the superposition principle, $h_1(x,y,t) = \int_{-\infty}^{0} g(x,t)e^{iqy}dq$, where q is the wavenumber which is related to the spatial period of the perturbation, l_w, by $q = 2\pi/l_w$. Each q can be considered separately due to the linearity of the system. Therefore, for a given q, we obtain the following equation for $g(x,t)$:

$$g_t = -\frac{\partial}{\partial x}\left[\left(h_0^3 + \frac{3\lambda\beta}{\lambda+2}h_0^{\lambda+2}\left(\Gamma^2\right)^{\frac{\lambda-1}{2}}\right)\left(\left(-D-q^2\right)g_x + g_{xxx}\right) + \left(3h_0^2 + 3\beta h_0^{\lambda+1}\left(\Gamma^2\right)^{\frac{\lambda-1}{2}}\right)\Gamma g\right] - \left(h_0^3 + \frac{3\lambda\beta}{\lambda+2}h_0^{\lambda+2}\left(\Gamma^2\right)^{\frac{\lambda-1}{2}}\right)\left(\left(Dq^2+q^4\right)g - q^2 g_{xx}\right) + Ug_x \quad (4.9)$$

$$\Gamma = \left(1 - Dh_{0x} + h_{0xxx}\right)$$

Here, subscripts x and t indicates partial derivatives. PDE's described in equation 4.8 and 4.9 were solved with grid spacing, $\Delta x = 0.01$. A mesh convergence study was performed to establish mesh independence of the solution. Second order central difference scheme was used to discretize the spatial variables and time integration was performed using Matlab's variable step ODE15s solver with default tolerance of 1E-6.

The perturbation function $g(x,t)$ has an exponential time dependence, $g(x,t) = \varphi(x)e^{\mu t}$ due to the homogeneity of Equation 4.9. Here, the quantity μ is known as the growth rate: small perturbations grow and develop patterns if μ is positive, whereas the imposed perturbations disappear if μ is negative. Once $g(x,t)$ for a particular wavenumber, q, is obtained by solving Equation 4.9, the growth rate, μ, can be calculated as:

$$\mu = \frac{1}{g}\frac{\partial g}{\partial t} \quad (4.10)$$

4.2.2 3D Nonlinear Simulation

Full nonlinear 3D simulation (2D spreading) were performed on a rectangular domain of size $L_x \times L_y$. Constant flux boundary condition was applied in the longitudinal or flow direction at $x = 0$ and $x = L_x$, while periodic boundary conditions were applied in the transverse direction at

$y = 0$ and $y = L_y$ [42]. For a single mode perturbation of wavelength l_w, the initial state was a step function with a slight perturbation of the contact line in the y direction given by

$$x = x_0 - 0.2\cos(2\pi y/l_w) \tag{4.11}$$

For simulating a random multimode perturbation, a 50 mode sinusoidal function was used to perturb the contact line:

$$x = x_0 - \sum_{i=1}^{50} A_i \cos\left(\frac{2\pi y}{l_{w,i}}\right) \tag{4.12}$$

Here, $l_{w,i} = 2L_y/i$, $i = 1, 2, \ldots 50$, and L_y is the length in the transverse direction which is same for all the simulations. The amplitudes $A_i$were random numbers between -0.2 and 0.2. All simulations were performed for a precursor film thickness, $b = 0.1$, and grid spacing, $\Delta x = 0.1, \Delta y = 0.1$. Second order central difference scheme was used to discretize the spatial variables and time integration was performed using Matlab's variable step ODE15s solver with default tolerance of 1E-6.

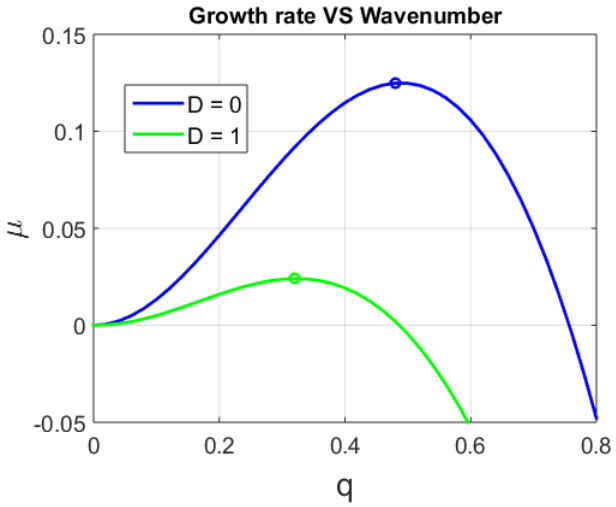

Figure 4.3. Growth rate curve of Newtonian thin films for $D = 0$, and $D = 1$. The markers represent the growth rate at the most unstable wavenumber. Precursor layer thickness of $b = 0.1$ was used.

4.3 Results and Discussion

4.3.1 Linear Stability Analysis

Figure 4.3 shows the growth rate curve of Newtonian thin films, and the results match with previously published results by Kondic [43]. The results also match with the Newtonian growth rate results published by Hu and Kieweg [45]. As can be seen from the figure, flatter inclination angle reduces the growth rate, tightens the band of unstable mode, and moves the most unstable mode to bigger wavelengths.

We present the results of linear stability analysis of Ellis thin films in Figure 4.4. Analysis was performed for vertical ($D = 0$) and shallow ($D = 1$) inclines. It can be seen that the growth rate of Ellis-type shear-thinning liquid films are functions of both the degree of shear-thinning, β, and the parameter for slope of the shear-thinning region, λ. As shown earlier in Figure 4.2, degree

of shear thinning $\beta = 0.1, 1$ and 10 was considered as progressively more shear thinning cases. Parameter $\lambda = 2$ and 3 were considered for slopes of shear-thinning. Here $\lambda = 3$ indicates a steeper slope compared to $\lambda = 2$ which results in a wider Newtonian plateau for the same value of β. For a smaller value of β, shear-thinning is mostly confined near the contact line region whereas for higher values of β, significant shear-thinning can occur far behind the contact line. As shown in Figure 4.2, for vertical incline ($D = 0$), the growth rate increases, and the band of unstable mode tightens with the increase in the degree of shear-thinning, β for both $\lambda = 2$ and 3. However, the growth rate for $\lambda = 3$ is lower due to the presence of wider Newtonian plateau, i.e. at lower values of shear stresses, the fluid with wider Newtonian plateau acts more Newtonian-like. No appreciable change in the most unstable mode is observed in either case. However, a slight shift in the most unstable wavenumber towards larger wavelength is observed for the $\beta = 10$ case while $\lambda = 2$. In comparison, the power-law model for $D = 0$, predicted a decrease in growth rate with increased shear-thinning and no change in the most unstable wavenumber [45].

For a flatter incline ($D = 1$), a shift in the most unstable wavenumber to larger wavelength was observed in all cases. For a shear-thinning fluid with wider Newtonian plateau ($\lambda = 3$), increasing the degree of shear-thinning decreases the growth rate and shifts the most unstable wavenumber to larger wavelength. As can be seen from the figure, $\beta = 10$ completely stabilizes the contact line. However, for shear-thinning fluids with a narrower Newtonian plateau ($\lambda = 2$), high degree of shear-thinning (large value of β) increases the growth rate despite the shift of the most unstable wavenumber towards larger wavelength. The shear-thinning of the fluid far behind the contact line is the probable cause of this phenomena. For highly shear-thinning fluids with a narrow Newtonian plateau, the apparent viscosity is significantly decreased far beyond the contact line. This increases the overall flow velocity of the liquid, which probably results in the increase in overall growth rate. In comparison, the power-law model for $D = 1$, predicted a decrease in growth rate with increased shear-thinning and no change in the most unstable

wavenumber [45]. These results highlight the complex behavior of contact line instability of shear-thinning fluids, when modeled by Ellis rheological model.

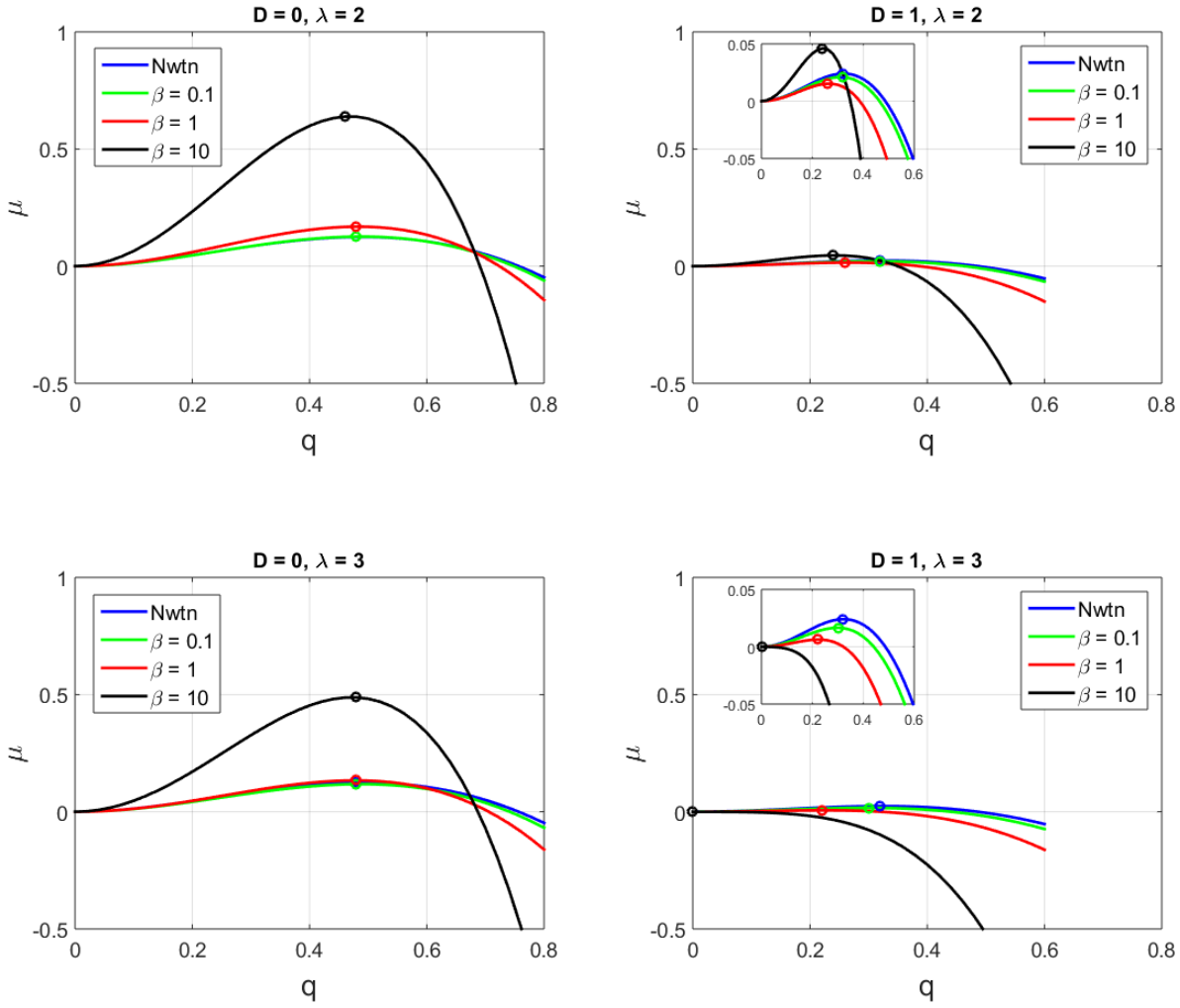

Figure 4.4. The growth rate $\mu(q)$ computed from long time behavior of solutions of linear PDE in Equation 4.9 for $D = 0,1$ and $\lambda = 2,3$. In each case, shear-thinning cases $\beta = 0.1,1,10$ were compared with the corresponding Newtonian case. The markers represent the growth rate at the most unstable wavenumber. Inset figures show a magnified view of the same results. Precursor film thickness $b = 0.1$ was used for all the cases.

4.3.2 Single Mode Perturbation and Comparison with LSA

We performed single finger evolution simulations to compare the growth rate from 3D nonlinear simulation with the growth rate obtained via linear stability analysis. The length in the transverse direction of the simulation domain were specified as equal to the most unstable wavenumbers from LSA. Perturbations were given following Equation 4.11. Figure 4.5 shows the evolution of a single finger over time as a representative case.

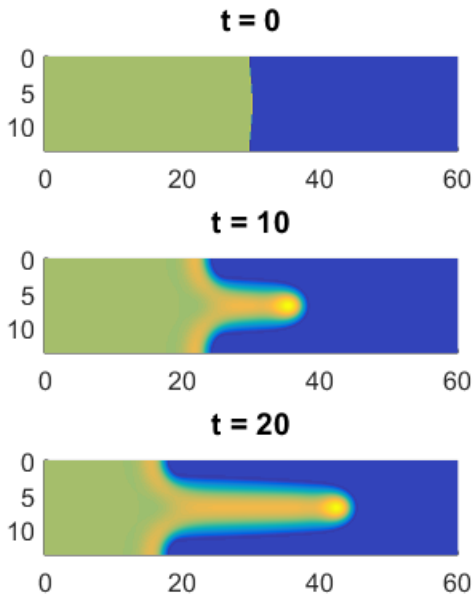

Figure 4.5. Evolution of a single finger for a shear thinning thin film with $D = 0, \beta = 10$ and $\lambda = 2$. Single mode perturbation was applied by making the transverse direction of the simulation domain L_y equal to the wavelength which was calculated from the most unstable wavenumber of LSA result ($q = 0.46, l_w = 2\pi/q = 13.7$).

Figure 4.6 quantitatively compares the growth rate of a single finger from 3D nonlinear simulation with growth rate obtained via LSA. The finger length L is the distance from the finger's tip to root, and is normalized with the initial finger length L_0 imposed by the initial perturbation.

The growth rates of LSA matches closely with the nonlinear simulation at early times. At later times, the finger growth slows down and approaches a lower constant speed since the overall travelling speed for a constant flux configuration is decided by the travelling wave speed. The results show that cases with higher growth rates deviate earlier from the LSA curve, indicating an earlier transition into the nonlinear regime.

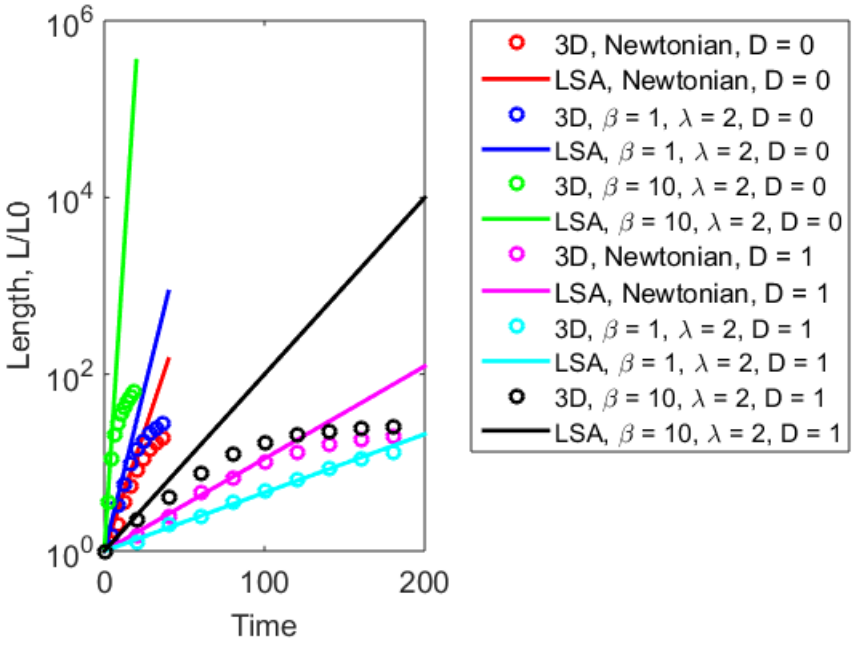

Figure 4.6. Comparison of growth rates from single mode perturbation simulation to the growth rate predicted by linear stability analysis.

4.3.3 Random Multimode Perturbation

We have also investigated the behavior of the contact line to randomly imposed multimode perturbation according to Equation 4.12, and compared them qualitatively with LSA results. Figure 4.7 shows the resulting fingers from the imposed perturbation for $D = 0$ and $\lambda = 2$. The Newtonian case is compared with shear-thinning cases of $\beta = 1$ and 10. It is obvious that the

growth rate increases (by observing finger length) with increased degree of shear-thinning, and highly shear-thinning fluids develop long and slender fingers very quickly.

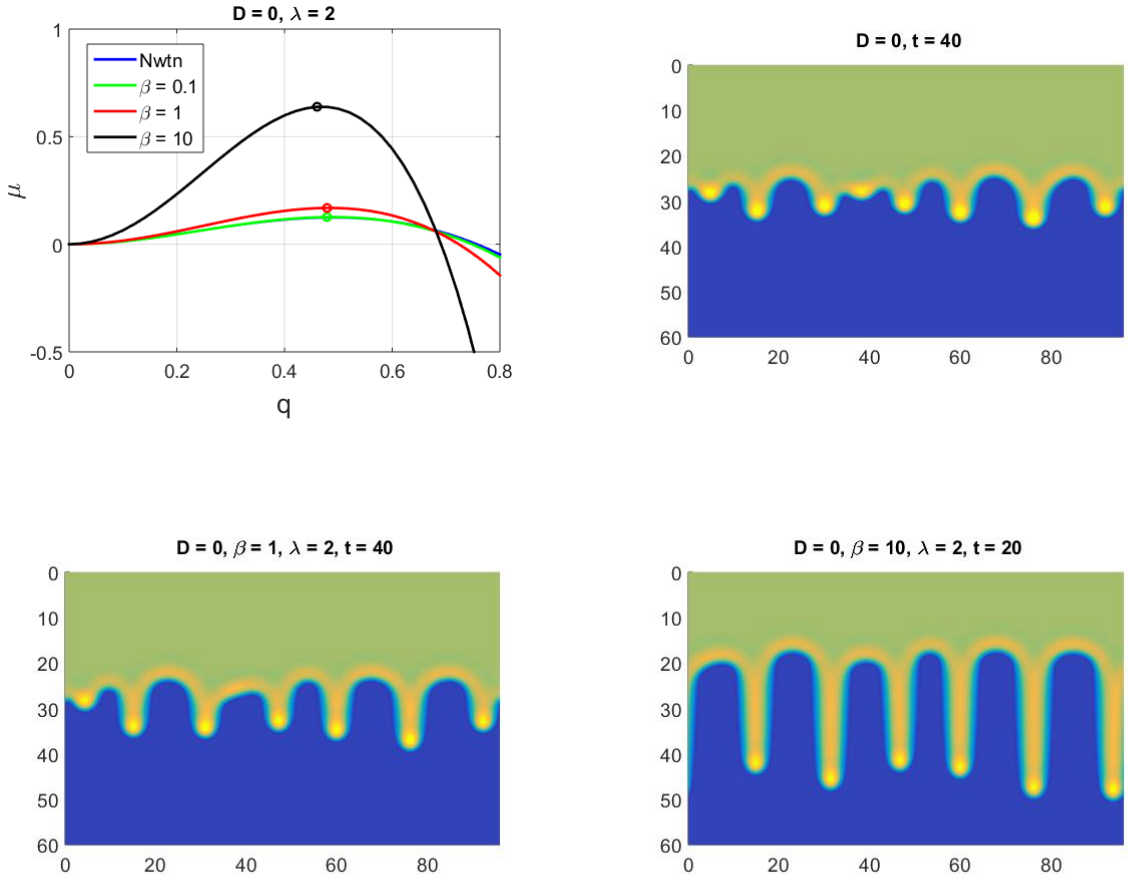

Figure 4.7. 3D simulation of random multimode perturbations for $D = 0$ and $\lambda = 2$. The Newtonian case is compared with shear-thinning cases of $\beta = 1$ and 10. Simulations were performed on a $L_x \times L_y = [60 \times 96]$ domain. Please note that the time of the snapshot for $\beta = 10$ case is at $t = 20$, whereas the other two cases are at $t = 40$ (because at $t = 40$, the finger would be longer than the simulation domain for $\beta = 10$).

Figure 4.8 shows the resulting fingers from randomly imposed perturbation for $D = 1$ and $\lambda = 2$. The Newtonian case is compared with shear-thinning cases of $\beta = 1$ and 10. The 3D simulations are in good agreement with the LSA results. Small degree of shear-thinning ($\beta = 1$)

seems to have reduced the growth rate. However, high degree of shear-thinning have reduced the number of fingers which is in agreement with the shift in the most unstable wavenumber to higher wavelength in the growth rate plot. There is also an increase in the growth of fingers which, as mentioned earlier, is probably a result of significant shear-thinning occurring far beyond the contact line. Similarly, good qualitative agreements with LSA results were also found for the $\lambda = 3$ cases (not shown here).

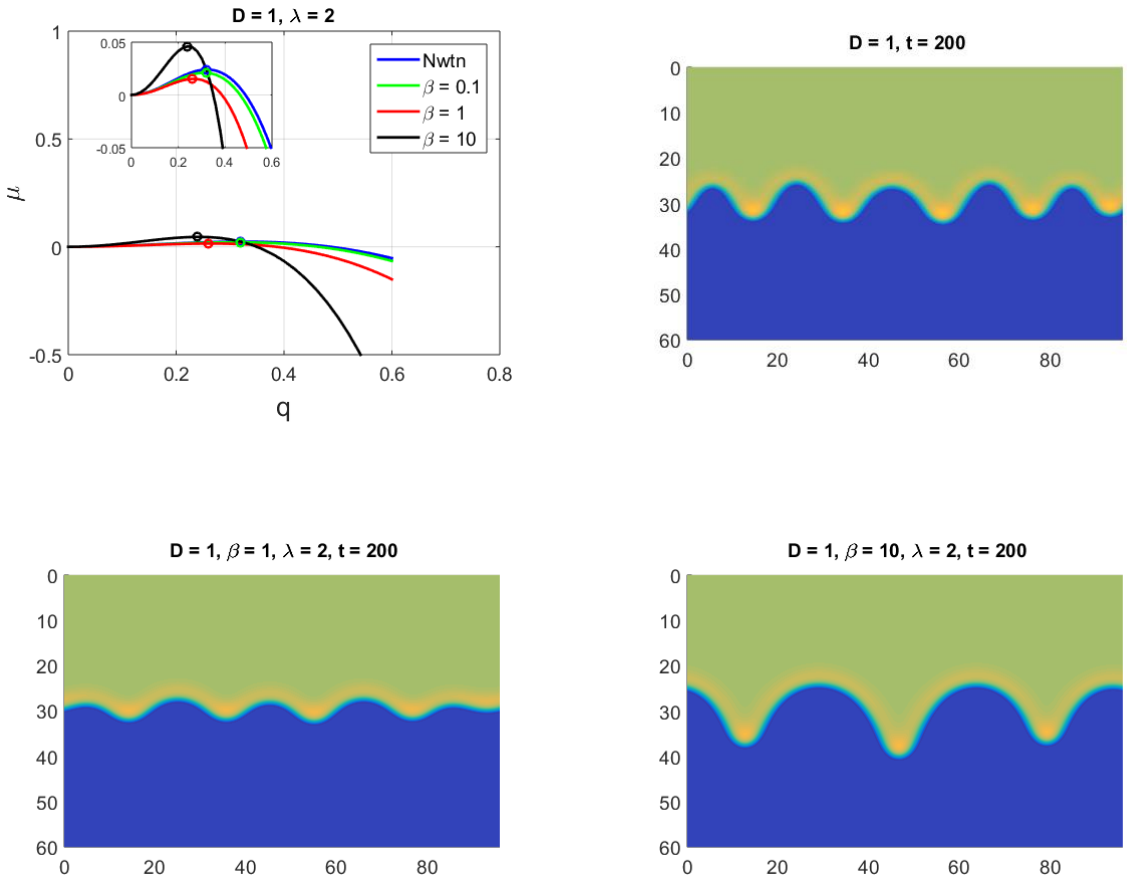

Figure 4.8. 3D simulation of random multimode perturbations for $D = 1$ and $\lambda = 2$. The Newtonian case is compared with shear-thinning cases of $\beta = 1$ and 10. Simulations were performed on a $L_x \times L_y = [60 \times 96]$ domain.

The typical initial distance between the finger-tips correspond to the most unstable wavelength. However, as the finger evolve and grow, they can merge to alter the initial spacing between finger-tips. Table 4.1 compares the characteristic finger wavelength obtained from 3D nonlinear simulation with the most unstable wavelength predicted by LSA. The finger wavelength was approximated by using the *findpeaks* function in Matlab®. The distance between all the adjacent finger-tips were obtained and averaged to get the value of the characteristic finger wavelength. The predicted wavelength from LSA was calculated as 2π divided by the most unstable wavenumber.

Table 4.1. A summary of the comparison between the most unstable wavelength obtained from LSA, and the characteristic finger wavelength obtained from 3D nonlinear simulation.

D	λ	Newtonian		β = 1		β = 10	
		LSA	3D	LSA	3D	LSA	3D
0	2	13.09	14.52	13.09	14.65	13.66	15.82
	3			13.09	14.65	13.09	15.70
1	2	19.63	19.78	24.17	19.45	26.18	21.00
	3			28.56	21.53	∞	∞

4.4 Conclusion

In this chapter, we have developed a model to study the contact line stability of gravity-driven thin film flow of Ellis-type shear-thinning fluid. The results have demonstrated a complex contact line behavior of Ellis-type fluid which is dependent on a combination of degree of shear-thinning and the slope of the shear-thinning region. Fluids with the same half shear stress, $\tau_{1/2}$ but different shear-thinning index, λ seems to have different behavior. There are lack of carefully

designed experimental studies which investigates the contact line behavior of gravity-driven thin film flow of shear-thinning fluids. It is crucial that we understand the contact line physics of shear-thinning fluids since shear-thinning fluids are common in many industrial and natural applications. Experimental studies will also help to resolve the discrepancies between the results in this chapter with the results found by Hu *et al.* for power-law fluids [45], which reported that contact lines are always stabilized due to shear-thinning.

In this chapter, we have considered a complete wetting scenario. Another natural extension of this study is the addition of a partially wetting contact line model similar to Eres *et al.* [63], in order to investigate how the shear-thinning affects the droplet pinch off behavior for sufficiently large contact angles.

Chapter 5

CONCLUSIONS AND FUTURE WORK

5.1 Summary

The broad goals of this dissertation were to (a) develop a mathematical model of boundary elasticity and gravity-driven thin film flow of Herschel-Bulkley fluids, (b) develop a mathematical model for rupture and dewetting of Ellis-type shear-thinning liquid films, and (c) develop a mathematical model for contact line instability of gravity-driven flow of Ellis-type thin liquid films.

The mathematical model of the squeezing flow of Herschel-Bulkley fluids has demonstrated the positive role that yield stress can play in controlling the spreading of the delivery vehicle. Our numerical models have suggested that yield stress can play a vital role during the early deployment time (2-5 minutes) by arresting the flow of the gel, and possibly also aid in retention of the gel in its intended location. We have demonstrated an optimization framework which can be used to design gel formulations and delivery location (along the vaginal axes) for women whose vaginal tissue elasticity may vary due to age or parity. We have assumed that vaginal tissue and the surrounding structure has isotropic material property to simplify the modeling process. We have also neglected the boundary dilution which may have only a minor affect during the early deployment times.

We have developed numerical models for modeling the rupture and dewetting process of Ellis-type shear-thinning fluids and compared the results with Newtonian fluid film dewetting. The rupture time study using 2D model have indicated that shear-thinning rheology accelerates the

rupture process. Simulations performed with the 2D model using different wavelengths of perturbation demonstrated that shear-thinning rheology has negligible effect on the preferred mode of instability, which corresponds to the initial spacing between the mounds or ridges. These characteristics were also observed in 3D simulations performed with random perturbation of the interface as shear-thinning rheology accelerated the rupture. The initial spacing between the mounds or ridges were also qualitatively similar between Newtonian and shear-thinning fluids, which verifies the finding from 2D simulation that the preferred mode of instability is similar for inelastic shear-thinning fluids compared to the Newtonian fluids.

Our study on the contact line instability of Ellis-type shear-thinning fluids have demonstrated the complex behavior of the contact line of shear-thinning fluids that are subjected to a perturbation at the moving front. For higher inclination angle, shear-thinning rheology increased the growth rate of fingers without any significant change in the most unstable mode. For low inclination angle, more complex behavior was observed. A low degree of shear-thinning stabilized the contact line and also shifted the most unstable mode to larger wavelength. However, for a high degree of shear-thinning fluid with small Newtonian plateau, the growth rate seems to increase even though the most unstable mode shifts toward larger wavelength. This could be attributed to the decrease in apparent viscosity far beyond the contact line, which increased the overall flow speed.

5.2 Future Work

Our optimization framework for estimating gel rheological properties can be extended in the future to a larger set of target gel functions (e.g. biocompatibility or anti-STI activity). While using this type of regression model based optimization, it is always important to ensure that an appropriate range of rheological properties, tissue elasticity, deployment time and initial bolus

volume is chosen for the model building set. Future studies may incorporate layers of different tissues (e.g. vaginal epithelium, smooth musculature, and underlying tissues such as bladder structures) in the surrounding “tissue” compartment of the model. Therefore, it is crucial that efforts are made towards developing new instruments so that vaginal mechanical properties could be measured *in vivo,* and the impact of the surrounding underlying tissues on the closing pressures of the vaginal tissue could be quantified and modeled. These measured properties can then be used in numerical models to study the deployment dynamics more accurately. The model could also incorporate boundary dilution in the future to investigate whether the effect of dilution is significant during the early stage deployment period.

Experimental investigation of rupture and dewetting process, and contact line instability of shear-thinning fluids should be performed in future to validate the findings from our numerical models. However, since shear-thinning fluids are described by multiple parameters (for example power-law having consistency and thinning index), it is difficult to synthesize multiple shear-thinning fluid samples where one parameter is constant but the other parameter is different. Mathematical models for rupture/dewetting of yield stress type fluids could also be developed in future to investigate whether yield stress has any stabilizing effect in case of film rupture. A regularized Bingham fluid model can be developed following the procedures described in Balmforth *et al*., [44]. A viscoelastic rupture/dewetting model could also be developed to study the effect of elasticity on film rupture, following the article published by Sapid and Homsy on contact line fingering of viscoelastic thin films [65]. A natural extension of the study on contact line instability would be to incorporate partial wetting in the model to investigate how shear-thinning rheology affects the pinch off behavior observed in films with high contact angle. The mathematical techniques developed as part of this dissertation can also be modified to study the evolution of shear-thinning droplets in order to investigate the effect of droplet size on the shape of the sliding/spreading drops and compare that with their Newtonian counterparts.

To summarize, these mathematical techniques are not specific to any single application. They can be modified and translated to numerous biological and industrial applications involving thin liquid films.

Appendix A1

Regression models for coating length and percentage yielding

The regression models used for optimizing the gel rheological properties in Chapter 2 are given in this section. These models correlate the coating length and percentage yielding with the gel rheological properties, tissue elasticity and deployment time.

A 1.1. Model for coating length

$$
\begin{aligned}
Coating\ length \\
&= 6.875 - 0.05986 \cdot m - 0.06847 \cdot \tau_0 + 0.1816 \cdot E + 0.01462 \cdot t + 0.01349 \cdot m \cdot n \\
&+ 0.00044 \cdot m \cdot \tau_0 - 0.0002888 \cdot m \cdot E + 0.00002795 \cdot m \cdot t - 0.009097 \cdot n \cdot \tau_0 \\
&+ 0.006034 \cdot n \cdot E + 0.006619 \cdot n \cdot t - 0.0003147 \cdot \tau_0 \cdot E - 0.0001388 \cdot \tau_0 \cdot t \\
&+ 0.0001238 \cdot E \cdot t + 0.0001746 \cdot m^2 - 0.2784 \cdot n^2 + 0.0003893 \cdot \tau_0^2 - 0.001456 \\
&\cdot E^2 - 0.00005235 \cdot t^2
\end{aligned}
$$

$$
adjusted\ R^2 = 0.9745, \quad Q^2 = 0.9744, \quad p - value < 2.2e - 16
$$

A 1.2. Model for percentage yielding

$$
\begin{aligned}
\%Yielding &= 76.45 + 0.704 \cdot m - 47.10 \cdot n - 1.801 \cdot \tau_0 + 0.4776 \cdot E - 0.1765 \cdot t - 0.2081 \cdot m \cdot n \\
&- 0.002518 \cdot m \cdot \tau_0 + 0.003108 \cdot m \cdot E - 0.0006389 \cdot m \cdot t + 0.1954 \cdot n \cdot \tau_0 \\
&+ 0.06795 \cdot n \cdot E - 0.06903 \cdot n \cdot t + 0.0006749 \cdot \tau_0 \cdot t - 0.00104 \cdot E \cdot t - 0.002236 \\
&\cdot m^2 + 24.3 \cdot n^2 + 0.01159 \cdot \tau_0^2 - 0.006644 \cdot E^2 + 0.0007944 \cdot t^2
\end{aligned}
$$

$$
adjusted\ R^2 = 0.9278, \quad Q^2 = 0.9275, \quad p - value < 2.2e - 16
$$

Appendix A2

Derivation of evolution equation for gravity and boundary elasticity driven squeezing flow of Herschel-Bulkley fluid

In this section, we provide detailed derivation of the evolution equation for gravity and boundary elasticity driven squeezing flow of Herschel-Bulkley fluids. For deriving the evolution equation given by Equation 2.2 in Chapter 2, we start from conservation of linear momentum in 3D, which is given by:

$$\rho\left(\vec{u}_t + \vec{u} \bullet \nabla\vec{u}\right) = -\nabla p + \nabla \bullet \tau + \rho g \tag{A2.1}$$

Here, ρ is density, g is gravitational acceleration, $\vec{u}$ is velocity vector, p is pressure, and $\boldsymbol{\tau}$ is stress tensor. By applying thin film lubrication approximation, inertial components can be neglected. For 2D flow (1D spreading) in xz plane, the momentum equation reduces to

$$0 = -\frac{\partial p}{\partial x} + \frac{\partial \tau_{xz}}{\partial z} + \rho g \tag{A2.2}$$

$$0 = -\frac{\partial p}{\partial z} \tag{A2.3}$$

Integrating equation A2.3, and applying boundary condition for pressure, p at the gel-tissue interface, $z = h(x,t)$, to be equal to, $p = Eh/T$, we get,

$$p = E\frac{h}{T} \tag{A2.4}$$

Here, E is the elasticity of the tissue, and T is the thickness of the tissue. Plugging in the value of p in equation A2.2, we get,

$$\frac{\partial \tau_{xz}}{\partial z} = \frac{E}{T}\frac{\partial h}{\partial x} - \rho g \tag{A2.5}$$

Integrating equation A2.5 with respect to z, and by applying zero shear stress boundary condition at the symmetry plane, $z = 0$, we get,

$$\tau_{xz} = \left(\frac{E}{T}\frac{\partial h}{\partial x} - \rho g\right) z \tag{A2.6}$$

At the yield surface where the shearing layer meets the plug layer ($z = h_0$), we have, $\tau_{xz} = \tau_0$. Therefore, from equation A2.6, we get the following expression for the height of the yield surface

$$h_0 = \frac{\tau_0}{\left(\frac{E}{T}\frac{\partial h}{\partial x} - \rho g\right)} \tag{A2.7}$$

The constitutive equation for Herchel-Bulkley fluid is given by,

$$\tau_{xz} = \tau_0 + m\left(\frac{\partial u}{\partial z}\right)^n \tag{A2.8}$$

Here, τ_0 is yield stress, m is consistency, and n is shear-thinning index. Combining equations A2.6, A2.7 and A2.8, we get an expression of $\partial u/\partial z$. Now, integrating with respect to z, and

applying a no-slip boundary condition at $z = h(x,t)$, we can arrive at the velocity of the yielding region

$$u = \left(\frac{1}{m}\right)^{1/n}\left(\frac{n}{1+n}\right)\left(\frac{E}{T}\frac{\partial h}{\partial x} - \rho g\right)^{1/n}\left[\left(z-h_0\right)^{\frac{1+n}{n}} - \left(h-h_0\right)^{\frac{1+n}{n}}\right] \qquad \text{for } h_0 < z < h \qquad \text{(A2.9)}$$

The velocity of the plug layer can be obtained by setting $z = h_0$ in equation A2.9. the velocity of plug layer u_p is given by,

$$u = \left(\frac{1}{m}\right)^{1/n}\left(\frac{n}{1+n}\right)\left(\frac{E}{T}\frac{\partial h}{\partial x} - \rho g\right)^{1/n}\left[-\left(h-h_0\right)^{\frac{1+n}{n}}\right] \qquad \text{(A2.10)}$$

Flow rate per unit width is given by the following expression

$$Q_x = h_0 u_p + \int_{h_0}^{h} u\,dz \qquad \text{(A2.11)}$$

Integral mass balance gives us the following form of evolution equation,

$$\frac{\partial h}{\partial t} + \frac{\partial Q_x}{\partial x} = 0 \qquad \text{(A2.12)}$$

Therefore, we get the PDE describing the evolution of Herschel-Bulkley thin film between elastic boundaries:

$$\frac{\partial h}{\partial t} + \frac{\partial}{\partial x}\left[\left(\frac{1}{m}\right)^{n}\left(\frac{n}{1+n}\right)\left(\frac{n}{1+2n}\right)\left(\frac{E}{T}\frac{\partial h}{\partial x} - \rho g\right)\left|\frac{E}{T}\frac{\partial h}{\partial x} - \rho g\right|^{\frac{1}{n}-1} Y^{\frac{1+n}{n}}\left(Y - \left(\frac{1+2n}{n}\right)h\right)\right] = 0 \qquad \text{(A2.13)}$$

$$Y = \max\left(h - \frac{\tau_0}{\left| \frac{E}{T}\frac{\partial h}{\partial x} - \rho g \right|}, 0 \right) \qquad \text{(A2.14)}$$

Appendix A3

Derivation of evolution equation for rupture of Ellis-type shear-thinning liquid films

In this section, we provide detailed derivation of the evolution equation for rupture and dewetting of Ellis-type shear-thinning liquid films. For deriving the dimensional evolution equation given by Equation 3.2 in Chapter 3, we start from conservation of linear momentum in 3D, which is given by:

$$\rho\left(\vec{u}_t + \vec{u} \bullet \nabla\vec{u}\right) = -\nabla p + \nabla \bullet \tau + \rho g \tag{A3.1}$$

Here, ρ is density, g is gravitational acceleration, $\vec{u}$ is velocity vector, p is pressure, and $\boldsymbol{\tau}$ is stress tensor. In this section, the bars used in chapter 3 to indicate dimensional quantity has been neglected for simplicity. By applying thin film lubrication approximation, inertial components can be neglected. Since we also neglect gravity, the conservation of linear momentum equation reduces to

$$0 = -\frac{\partial p}{\partial x} + \frac{\partial \tau_{xz}}{\partial z} \tag{A3.2}$$

$$0 = -\frac{\partial p}{\partial y} + \frac{\partial \tau_{yz}}{\partial z} \tag{A3.3}$$

$$0 = -\frac{\partial p}{\partial z} \tag{A3.4}$$

The pressure in the fluid is given by

$$p = -\sigma \nabla^2 h - \Pi \tag{A3.5}$$

Here, σ is the surface tension, $\nabla^2 h$ is the small slope approximation of the free surface curvature, and Π is the disjoining pressure. Integrating equation A3.2 and A3.3 with respect to z, and by applying zero shear stress at the free surface, $z = h$, we get the expression of shear stresses

$$\tau_{xz} = -\frac{\partial p}{\partial x}(h - z) \tag{A3.6}$$

$$\tau_{yz} = -\frac{\partial p}{\partial y}(h - z) \tag{A3.7}$$

The Ellis constitutive model is given by

$$\frac{1}{\eta} = \frac{1}{\eta_0}\left(1 + \left|\frac{\sqrt{\tau_{xz}^{\ 2} + \tau_{yz}^{\ 2}}}{\tau_{1/2}}\right|^{\lambda - 1}\right) \tag{A3.8}$$

Here, η is the viscosity, η_0 is the viscosity at zero shear stress, $\tau_{1/2}$ is the shear-stress at which the viscosity is reduced by half, and λ is the shear-thinning index. The relevant components of stress tensor are given by

$$\tau_{xz} = \eta \frac{\partial u}{\partial z} \tag{A3.9}$$

$$\tau_{yz} = \eta \frac{\partial v}{\partial z} \tag{A3.10}$$

Combining equation A3.6 to A3.10, we can obtain expressions of $\partial u/\partial z$ and $\partial v/\partial z$. Now, integrating with respect to z, and applying a no-slip boundary condition at $z = 0$, we arrive at expressions of velocity

$$u = \frac{T_1}{\eta_0}\left(hz - \frac{z^2}{2} + \left(\frac{\sqrt{T_1^{\,2} + T_2^{\,2}}}{\tau_{1/2}} \right)^{\lambda - 1} \frac{h^{\lambda+1} - (h-z)^{\lambda+1}}{\lambda + 1} \right) \tag{A3.11}$$

$$v = \frac{T_2}{\eta_0}\left(hz - \frac{z^2}{2} + \left(\frac{\sqrt{T_1^{\,2} + T_2^{\,2}}}{\tau_{1/2}} \right)^{\lambda - 1} \frac{h^{\lambda+1} - (h-z)^{\lambda+1}}{\lambda + 1} \right) \tag{A3.12}$$

Where,

$$T_1 = \frac{\partial}{\partial x}\left(\sigma \nabla^2 h + \Pi \right) \qquad T_2 = \frac{\partial}{\partial y}\left(\sigma \nabla^2 h + \Pi \right) \tag{A3.13}$$

The flow rates are given by

$$Q_x = \int_0^h u dz \qquad Q_y = \int_0^h v dz \tag{A3.14}$$

Finally, the evolution equation obtained from integral mass balance is given by

$$\frac{\partial h}{\partial t} = -\frac{1}{3\eta_0}\left(\frac{\partial Q_x}{\partial x} + \frac{\partial Q_y}{\partial y} \right) \tag{A3.15}$$

$$Q_x = h^3 \frac{\partial}{\partial x}\left(\sigma\nabla^2 h + \Pi\right)F \tag{A3.16}$$

$$Q_y = h^3 \frac{\partial}{\partial y}\left(\sigma\nabla^2 h + \Pi\right)F \tag{A3.17}$$

$$F = 1 + \frac{3}{\lambda+2}\left(\frac{h}{\tau_{1/2}}\right)^{\lambda-1}\left(\left[\frac{\partial}{\partial x}\left(\sigma\nabla^2 h + \Pi\right)\right]^2 + \left[\frac{\partial}{\partial y}\left(\sigma\nabla^2 h + \Pi\right)\right]^2\right)^{\frac{\lambda-1}{2}} \tag{A3.18}$$

Appendix A4

Derivation of evolution equation for gravity-driven thin film flow of Ellis-type shear-thinning liquid

In this section, we provide detailed derivation of the evolution equation for gravity-driven thin film flow of Ellis-type shear-thinning liquids. For deriving the dimensional evolution equation of thin film on an incline (with an angle α with horizontal) given by Equation 4.2 in Chapter 4, we start from conservation of linear momentum in 3D, which is given by:

$$\rho\left(\vec{u}_t + \vec{u} \bullet \nabla \vec{u}\right) = -\nabla p + \nabla \bullet \tau + \rho g \tag{A4.1}$$

Here, ρ is density, g is gravitational acceleration, $\vec{u}$ is velocity vector, p is pressure, and $\boldsymbol{\tau}$ is stress tensor. In this section, the bars used in chapter 4 to indicate dimensional quantity has been neglected for simplicity. By applying thin film lubrication approximation, inertial components can be neglected. The conservation of linear momentum equation reduces to

$$0 = -\frac{\partial p}{\partial x} + \frac{\partial \tau_{xz}}{\partial z} + \rho g \sin\alpha \tag{A4.2}$$

$$0 = -\frac{\partial p}{\partial y} + \frac{\partial \tau_{yz}}{\partial z} \tag{A4.3}$$

$$0 = -\frac{\partial p}{\partial z} - \rho g \cos\alpha \tag{A4.4}$$

The pressure in the fluid can be obtained by integrating equation A4.4 and applying boundary condition, $p = -\sigma\nabla^2 h + p_0$, at $z = h$, we get,

$$p = \rho g \cos\alpha (h - z) - \sigma\nabla^2 h + p_0 \tag{A4.5}$$

Here, σ is the surface tension, $\nabla^2 h$ is the small slope approximation of the free surface curvature, and p_0 is the atmospheric pressure. Integrating equation A4.2 and A4.3 with respect to z, and by applying zero shear stress at the free surface, $z = h$, we get the expression of shear stress

$$\tau_{xz} = \left[\rho g \sin\alpha - \rho g \cos\alpha \frac{\partial h}{\partial x} + \sigma \frac{\partial}{\partial x}\left(\nabla^2 h\right) \right](h - z) = T_1(h - z) \tag{A4.6}$$

$$\tau_{yz} = \left[-\rho g \cos\alpha \frac{\partial h}{\partial y} + \sigma \frac{\partial}{\partial y}\left(\nabla^2 h\right) \right](h - z) = T_2(h - z) \tag{A4.7}$$

The Ellis constitutive model is given by

$$\frac{1}{\eta} = \frac{1}{\eta_0}\left(1 + \left| \frac{\sqrt{{\tau_{xz}}^2 + {\tau_{yz}}^2}}{\tau_{1/2}} \right|^{\lambda - 1} \right) \tag{A4.8}$$

Here, η is the viscosity, η_0 is the viscosity at zero shear stress, $\tau_{1/2}$ is the shear-stress at which the viscosity is reduced by half, and λ is the shear-thinning index. The relevant components of stress tensor are given by

$$\tau_{xz} = \eta \frac{\partial u}{\partial z} \tag{A4.9}$$

$$\tau_{yz} = \eta \frac{\partial v}{\partial z} \tag{A4.10}$$

Combining equation A4.6 to A4.10, we can obtain expressions of $\partial u/\partial z$ and $\partial v/\partial z$. Now, integrating with respect to z, and applying a no-slip boundary condition at $z = 0$, we arrive at expressions of velocity

$$u = \frac{T_1}{\eta_0}\left(hz - \frac{z^2}{2} + \left(\frac{\sqrt{T_1^{\,2} + T_2^{\,2}}}{\tau_{1/2}} \right)^{\lambda-1} \frac{h^{\lambda+1} - (h-z)^{\lambda+1}}{\lambda+1} \right) \tag{A4.11}$$

$$v = \frac{T_2}{\eta_0}\left(hz - \frac{z^2}{2} + \left(\frac{\sqrt{T_1^{\,2} + T_2^{\,2}}}{\tau_{1/2}} \right)^{\lambda-1} \frac{h^{\lambda+1} - (h-z)^{\lambda+1}}{\lambda+1} \right) \tag{A4.12}$$

The flow rates are given by

$$Q_x = \int_0^h u dz \qquad\qquad Q_y = \int_0^h v dz \tag{A4.15}$$

Finally, the evolution equation obtained from integral mass balance is given by

$$\frac{\partial h}{\partial t} = -\frac{1}{3\eta_0}\left(\frac{\partial Q_x}{\partial x} + \frac{\partial Q_y}{\partial y} \right) \tag{A4.16}$$

$$Q_x = h^3 \left[\rho g \sin\alpha - \rho g \cos\alpha \frac{\partial h}{\partial x} + \sigma \frac{\partial}{\partial x}\left(\nabla^2 h \right) \right] F \tag{A4.17}$$

$$Q_y = h^3\left[-\rho g\cos\alpha\frac{\partial h}{\partial y}+\sigma\frac{\partial}{\partial y}\left(\nabla^2 h\right)\right]F \tag{A4.18}$$

$$\bar{F} = 1+\frac{3}{\lambda+2}\left(\frac{\bar{h}}{\tau_{1/2}}\right)^{\lambda-1}\left(\left[\rho g\alpha\sin\alpha-\rho g\cos\alpha\frac{\partial\bar{h}}{\partial\bar{x}}+\sigma\frac{\partial}{\partial\bar{x}}\left(\nabla^2\bar{h}\right)\right]^2+\left[-\rho g\cos\alpha\frac{\partial\bar{h}}{\partial\bar{y}}+\sigma\frac{\partial}{\partial\bar{y}}\left(\nabla^2\bar{h}\right)\right]^2\right)^{\frac{\lambda-1}{2}} \tag{A4.19}$$

References

[1] Hu B, Kieweg SL. The effect of surface tension on the gravity-driven thin film flow of Newtonian and power-law fluids. Computers & Fluids. 2012;64:83-90.

[2] Kheyfets VO, Kieweg SL. Gravity-driven thin film flow of an ellis fluid. Journal of Non-Newtonian Fluid Mechanics. 2013;202:88-98.

[3] Kheyfets VO, Kieweg SL. Experimental and numerical models of three-dimensional gravity-driven flow of shear-thinning polymer solutions used in vaginal delivery of microbicides. Journal of biomechanical engineering. 2013;135:061009.

[4] Szeri AJ, Park SC, Verguet S, Weiss A, Katz DF. A model of transluminal flow of an anti-HIV microbicide vehicle: Combined elastic squeezing and gravitational sliding. Physics of Fluids. 2008;20.

[5] Tasoglu S, Katz DF, Szeri AJ. Transient spreading and swelling behavior of a gel deploying an anti-HIV topical microbicide. Journal of Non-Newtonian Fluid Mechanics. 2012;187:36-42.

[6] Tasoglu S, Park SC, Peters JJ, Katz DF, Szeri AJ. The consequences of yield stress on deployment of a non-Newtonian anti-HIV microbicide gel. Journal of Non-Newtonian Fluid Mechanics. 2011;166:1116-22.

[7] Gouldstone A, Brown RE, Butler JP, Loring SH. Elastohydrodynamic separation of pleural surfaces during breathing. Respiratory Physiology & Neurobiology. 2003;137:97-106.

[8] Jin ZM, Dowson D. Elastohydrodynamic lubrication in biological systems. Proceedings of the Institution of Mechanical Engineers Part J-Journal of Engineering Tribology. 2005;219:367-80.

[9] Jones MB, Fulford GR, Please CP, McElwain DLS, Collins MJ. Elastohydrodynamics of the eyelid wiper. Bulletin of Mathematical Biology. 2008;70:323-43.

[10] Jossic L, Lefevre P, de Loubens C, Magnin A, Corre C. The fluid mechanics of shear-thinning tear substitutes. Journal of Non-Newtonian Fluid Mechanics. 2009;161:1-9.

[11] Wilson S, Burgess S. The steady, spreading flow of a rivulet of mud. Journal of Non-Newtonian Fluid Mechanics. 1998;79:77-85.

[12] Svendsen B, Wu T, Johnk K, Hutter K. On the role of mechanical interactions in the steady-state gravity flow of a two-constituent mixture down an inclined plane. Proceedings of the Royal Society of London A: Mathematical, Physical and Engineering Sciences. 1996;452:1189-205.

[13] Evans P, Schwartz L, Roy R. A mathematical model for crater defect formation in a drying paint layer. Journal of colloid and interface science. 2000;227:191-205.

[14] Mirle SK, Zettlemoyer A. Viscoelasticity of photopolymer plates and ink hydrodynamics in modelling flexographic printing. Mathematical and Computer Modelling. 1988;11:1162-5.

[15] Yonkoski R, Soane D. Model for spin coating in microelectronic applications. Journal of applied physics. 1992;72:725-40.

[16] Bertozzi AL, Brenner MP. Linear stability and transient growth in driven contact lines. Physics of Fluids (1994-present). 1997;9:530-9.

[17] Burelbach JP, Bankoff SG, Davis SH. Nonlinear stability of evaporating/condensing liquid films. Journal of Fluid Mechanics. 1988;195:463-94.

[18] Huppert HE. Flow and instability of a viscous current down a slope. Nature. 1982;300:427-9.

[19] HIV/AIDS JUNPo. Global report: UNAIDS report on the global AIDS epidemic: 2012. UNAIDS; 2012.

[20] Cohen MS. Amplified transmission of HIV-1: missing link in the HIV pandemic. Transactions of the American Clinical and Climatological Association. 2006;117:213.

[21] Cohen MS, Hoffman IF, Royce RA, Kazembe P, Dyer JR, Daly CC, et al. Reduction of concentration of HIV-1 in semen after treatment of urethritis: implications for prevention of sexual transmission of HIV-1. The Lancet. 1997;349:1868-73.

[22] Karim QA. Effectiveness and safety of tenofovir gel, an antiretroviral microbicide, for the prevention of HIV infection in women (September, pg 1168, 2010). Science. 2011;333:524-.

[23] Kieweg SL, Geonnotti AR, Katz DF. Gravity-induced coating flows of vaginal gel formulations: In vitro experimental analysis. Journal of Pharmaceutical Sciences. 2004;93:2941-52.

[24] Groups MW. The Microbicide Development Strategy. Silver Spring, MD,USA: Alliance for Microbicide Development; 2006.

[25] Kieweg SL, Katz DF. Squeezing flows of vaginal gel formulations relevant to microbicide drug delivery. Journal of Biomechanical Engineering-Transactions of the ASME. 2006;128:540-53.

[26] Kieweg SL, Katz DF. Interpreting properties of microbicide drug delivery gels: analyzing deployment kinetics due to squeezing. Journal of Pharmaceutical Sciences. 2007;96:835-50.

[27] Owen DH, Peters JJ, Kieweg SL, Geonnotti AR, Schnaare RL, Katz DF. Biophysical analysis of prototype microbicidal gels. Journal of Pharmaceutical Sciences. 2007;96:661-9.

[28] Acheson DJ. Elementary fluid dynamics: Oxford University Press; 1990.

[29] Jensen O, Grotberg J. Insoluble surfactant spreading on a thin viscous film: shock evolution and film rupture. Journal of Fluid Mechanics. 1992;240:259-88.

[30] Krebs FC. Fabrication and processing of polymer solar cells: a review of printing and coating techniques. Solar energy materials and solar cells. 2009;93:394-412.

[31] Sharma A, Ruckenstein E. Mechanism of tear film rupture and formation of dry spots on cornea. Journal of colloid and interface science. 1985;106:12-27.

[32] Tracton AA. Coatings technology handbook: CRC press; 2005.

[33] Zhang Z, Wang Z, Xing R, Han Y. Patterning thin polymer films by surface-directed dewetting and pattern transfer. Polymer. 2003;44:3737-43.

[34] Yiantsios SG, Higgins BG. Rupture of thin films: Nonlinear stability analysis. Journal of colloid and interface science. 1991;147:341-50.

[35] Schwartz LW, Roy RV, Eley RR, Petrash S. Dewetting patterns in a drying liquid film. Journal of colloid and interface science. 2001;234:363-74.

[36] Ajaev VS. Evolution of dry patches in evaporating liquid films. Physical Review E. 2005;72:031605.

[37] Ajaev VS. Effect of nanoscale bubbles on viscous flow and rupture in thin liquid films. Physics of Fluids (1994-present). 2006;18:068101.

[38] Thiele U, Vancea I, Archer AJ, Robbins MJ, Frastia L, Stannard A, et al. Modelling approaches to the dewetting of evaporating thin films of nanoparticle suspensions. Journal of Physics: Condensed Matter. 2009;21:264016.

[39] Bird RB, Armstrong R, Hassager O. Dynamics of polymeric liquids. Vol. 1: Fluid mechanics1987.

[40] Diez JA, Kondic L, Bertozzi A. Global models for moving contact lines. Physical Review E. 2000;63:011208.

[41] Kondic L, Bertozzi A. Nonlinear dynamics and transient growth of driven contact lines. Physics of Fluids (1994-present). 1999;11:3560-2.

[42] Kondic L, Diez J. Pattern formation in the flow of thin films down an incline: Constant flux configuration. Physics of Fluids (1994-present). 2001;13:3168-84.

[43] Kondic L. Instabilities in gravity driven flow of thin fluid films. Siam Review. 2003;45:95-115.

[44] Balmforth N, Ghadge S, Myers T. Surface tension driven fingering of a viscoplastic film. Journal of Non-Newtonian Fluid Mechanics. 2007;142:143-9.

[45] Hu B, Kieweg SL. Contact line instability of gravity-driven flow of power-law fluids. Journal of Non-Newtonian Fluid Mechanics. 2015;225:62-9.

[46] Balmforth N, Craster R. A consistent thin-layer theory for Bingham plastics. Journal of Non-Newtonian Fluid Mechanics. 1999;84:65-81.

[47] Egorov V, Sarvazyan AP. Methods for characterizing vaginal tissue elasticity. US8052622 B2; 2011.

[48] Katz DF, Gao Y, Kang M. Using modeling to help understand vaginal microbicide functionality and create better products. Drug delivery and translational research. 2011;1:256-76.

[49] Rohan LC, Sassi AB. Vaginal drug delivery systems for HIV prevention. The AAPS journal. 2009;11:78-87.

[50] Mahalingam A, Smith E, Fabian J, Damian FR, Peters JJ, Clark MR, et al. Design of a semisolid vaginal microbicide gel by relating composition to properties and performance. Pharmaceutical research. 2010;27:2478-91.

[51] Corporation GD. General Algebraic Modeling System (GAMS) Release 24.2.1. Washington, DC, USA2013.

[52] Vrij A, Overbeek JT. Rupture of thin liquid films due to spontaneous fluctuations in thickness. Journal of the American Chemical Society. 1968;90:3074-+.

[53] Erneux T, Davis SH. Nonlinear rupture of free films. Physics of Fluids A: Fluid Dynamics (1989-1993). 1993;5:1117-22.

[54] Frumkin A. On the wetting phenomena and attachment of bubbles. Zhur Fiz Khim(J Phys Chem). 1938;12:337-45.

[55] Derjaguin B. Theory of the capillary condensation and other capillary phenomena taking into account the disjoining effect of long-chain molecular liquid films. Zh Fiz Khim. 1940;14:137.

[56] Schwartz LW. Hysteretic effects in droplet motions on heterogeneous substrates: direct numerical simulation. Langmuir. 1998;14:3440-53.

[57] Braun R, Usha R, McFadden G, Driscoll T, Cook L, King-Smith PE. Thin film dynamics on a prolate spheroid with application to the cornea. Journal of Engineering Mathematics. 2012;73:121-38.

[58] Ajaev VS. Interfacial fluid mechanics: Springer; 2012.

[59] Lade RK, Song JO, Musliner AD, Williams BA, Kumar S, Macosko CW, et al. Sag in drying coatings: Prediction and real time measurement with particle tracking. Progress in Organic Coatings. 2015;86:49-58.

[60] Espín L, Kumar S. Sagging of evaporating droplets of colloidal suspensions on inclined substrates. Langmuir. 2014;30:11966-74.

[61] Anwar MR, Camarda KV, Kieweg SL. Mathematical model of microbicidal flow dynamics and optimization of rheological properties for intra-vaginal drug delivery: role of tissue mechanics and fluid rheology. Journal of biomechanics. 2015;48:1625-30.

[62] Troian S, Herbolzheimer E, Safran S, Joanny J. Fingering instabilities of driven spreading films. EPL (Europhysics Letters). 1989;10:25.

[63] Eres M, Schwartz L, Roy R. Fingering phenomena for driven coating films. Physics of Fluids (1994-present). 2000;12:1278-95.

[64] Spaid M, Homsy G. Stability of Newtonian and viscoelastic dynamic contact lines. Physics of Fluids (1994-present). 1996;8:460-78.

[65] Spaid M, Homsy G. Stability of viscoelastic dynamic contact lines: An experimental study. Physics of Fluids (1994-present). 1997;9:823-32.

[66] Dussan E. On the spreading of liquids on solid surfaces: static and dynamic contact lines. Annual Review of Fluid Mechanics. 1979;11:371-400.